






Article

Holocene Paleoenvironmental Evolution of a Semi-Enclosed Shallow Aegean Basin: A Combination of Seismic Stratigraphy and Sediment Core Proxies

Alexandra Noti ¹, Lucas J. Lourens ², Maria Geraga ^{1,*}, Frank P. Wesselingh ^{2,3}, Negar Haghipour ⁴, Nikos Georgiou ^{1,5}, Dimitris Christodoulou ¹, Spyros Sergiou ¹, Xenophon Dimas ¹, Andreas G. Vlachopoulos ⁶ and George Papatheodorou ¹

¹ Laboratory of Marine Geology and Physical Oceanography, Department of Geology, University of Patras, 26500 Rio, Greece

² Department of Earth Sciences, Faculty of Geosciences, Utrecht University, 3584 Utrecht, The Netherlands

³ Naturalis Biodiversity Center, 2300 Leiden, The Netherlands

⁴ Laboratory of Ion Beam Physics, Geological Institute, ETH Zürich, 8092 Zürich, Switzerland

⁵ Department of Environmental Sciences, Informatics and Statistics, Ca' Foscari University, 30170 Venice, Italy

⁶ Department of History and Archaeology, University of Ioannina, 45110 Ioannina, Greece

* Correspondence: mgeraga@upatras.gr; Tel.: +30-2610997412



Citation: Noti, A.; Lourens, L.J.; Geraga, M.; Wesselingh, F.P.; Haghipour, N.; Georgiou, N.; Christodoulou, D.; Sergiou, S.; Dimas, X.; Vlachopoulos, A.G.; et al. Holocene Paleoenvironmental Evolution of a Semi-Enclosed Shallow Aegean Basin: A Combination of Seismic Stratigraphy and Sediment Core Proxies. *Water* **2022**, *14*, 3688. <https://doi.org/10.3390/w14223688>

Academic Editor: Luisa Bergamin

Received: 6 October 2022

Accepted: 9 November 2022

Published: 15 November 2022

Publisher's Note: MDPI stays neutral with regard to jurisdictional claims in published maps and institutional affiliations.



Copyright: © 2022 by the authors. Licensee MDPI, Basel, Switzerland. This article is an open access article distributed under the terms and conditions of the Creative Commons Attribution (CC BY) license (<https://creativecommons.org/licenses/by/4.0/>).

Abstract: The island of Astypalea (Greece), known for its rich and pristine archeological sites, encompasses a semi-enclosed silled basin that has been very susceptible to global sea levels and regional climate changes due to its relatively modern shallow sill of 4.7 m water deep that connects the Vathy bay with the adjacent Aegean Sea. To identify the causal relationship between regional climate, sea-level trajectories, and environmental change and their potential impact on hominine habitats on the island, we investigated a high-resolution seismic profile together with sediment, stable isotope, geochemical, and biotic proxies retrieved from a marine sediment core (ASTC1). Our results show that the basin was once isolated, and a marine inundation occurred at around 7.3 ka BP, which is older than expected, based on global sea level reconstructions. The entire transition from isolation to full marine conditions was accomplished in three major phases: (1) non-marine isolated conditions between 9–7.3 ka BP, (2) semi-isolated hypersaline marsh and lagoonal conditions between 7.3 and 4.1 ka BP, and (3) semi-isolated shallow marine conditions of today (4.1 ka BP to present). High water alkalinity, elevated organic content, and heavier isotopic signals indicate relatively arid conditions in the region that favored Sr-rich carbonate precipitation within the 7.3–6 ka BP interval. On the other hand, freshwater biota, along with a high C_{org}/N ratio and lighter isotopic signal, showed wetter conditions, at least for the intervals 8–7.3 ka and 6–5.4 ka BP, in contrast to the aridification trend seen as 4.1 ka to present. Finally, the hominine habitat evolution at around 6 ka BP might be attributed to the wetter conditions and the freshwater source provided by the bay at that time.

Keywords: Holocene; stable isotopes; seismic stratigraphy; climatic change; Eastern Mediterranean

1. Introduction

Holocene climatic variation in the eastern Mediterranean (EM) region is attributed to both changes in the high latitude [1,2] and the African monsoon (AM) intensity [3–5]. Northerly cold polar/continental air outbreaks at times of intensified Siberian high pressure seem to be responsible for the prevalence of Holocene cold events [2].

The best documented links between the Mediterranean climate and the southern monsoonal system concern precipitation maxima linked to increased river outflows triggered by a monsoonal intensification over north Africa between 9 and 6 ka BP [6]. The consequent alternations of the EM oceanographic regime triggered the deposition of the sapropel layer in the marine realm, a layer that is basically recognized by the high organic carbon content in the marine sediments (>2%, [7]).

Most of the above-mentioned knowledge originates from studies on deep water marine sediments from sites deeper than 200–300 m water depth in the EM [8–11]. These sites remained underwater even during the Last Glacial Maximum (LGM) when the sea level reached the lowest point of 125 m below the present, whereas the sites shallower than 125 m experienced subaerial conditions [12]. The end of the last glacial period was accompanied by general climatic improvement and continuous sea level rise, which finally contributed to significant alternations of the coastal landscape and the gradual submergence of the ancient coastal zone [13–16]. This transition has been well documented in the EM, particularly in its northern parts (Aegean, Ionian, and Adriatic Seas), which have a complex basin topography [16–22]. Rates of the Holocene sea level rise were initially rapid (global mean sea level rose from 61 m to 4 m below present-day sea level) between 11.7 ka BP and 6.7 ka BP [23]. Regional sea-level rise and coastal drowning trajectories are affected by additional isostatic [24] and tectonic factors [13,25–29].

Depending on the local topography, geology, and hydrodynamics, the transgression resulted in the formation of a dynamic range of successive environments ranging from lowlands to lagoons and shallow bays, as well as deeper shelf settings [13,14,16]. The development of shallow marine habitats, such as lagoons and semi-enclosed bays, was driven by topographic configuration (including sill depths), sediment, freshwater, and organic supply. These resulted in a succession of abiotic (lithology, [30,31]) organic and inorganic chemistry and minerals [16,31], oceanography [5,32], and biotic (faunal [33,34] and floral [35]) conditions. Sediments deposited in favorable sites can store informative proxies regarding the variation of the above-mentioned parameters and serve as archives for predicting the evolution of the environment, the climate, and the relative sea level changes of the examined area over time [24].

In this paper, we present the results of sedimentological analyses conducted on a 3.2 m long sediment core (ASTC1) collected from Vathy bay, a silled-semi enclosed bay in Astypalea island (Figure 1) that represents such an optimal sedimentary archive. The sediment core spans the middle and late Holocene epochs. We obtained a high-resolution dataset including grain size, sediment color, geochemistry, stable isotope, and foraminifera and mollusk data. The wider deposition of the core was examined using new seismic profiles, and stratigraphic ages were constrained through new radiocarbon dates.

Astypalea island is located in the south-eastern Aegean Sea, a seismically active region [36] (Figure 1). The Vathy bay is currently connected to the open sea via a narrow and shallow strait of about 4.7 m depth. The shallow sill depth and active regional tectonism make this area very susceptible to Holocene Sea level variations. The scope of this study is to document landscape successions and link them to sea-level change and direct climate change. Taking into consideration that the site is situated in the Mediterranean Sea, a basin characterized by high surface salinities [37], the findings of the present study are expected to contribute to relative studies on shelf environments in evaporative basins. The Vathy bay is a site of great archaeological importance: on-land archaeological surveying has shown continued occupation since at least Late Neolithic times [38]. Understanding successive landscape configurations and abiotic characteristics will help to assess the potential for human exploitation of the environment. Over Neolithic times, the coastal zone was always the most populated area worldwide [14,39,40], and thus, the outcome of this research is expected to contribute to studies that focus on the understanding of the human response and adaption to an alterable coastal landscape.

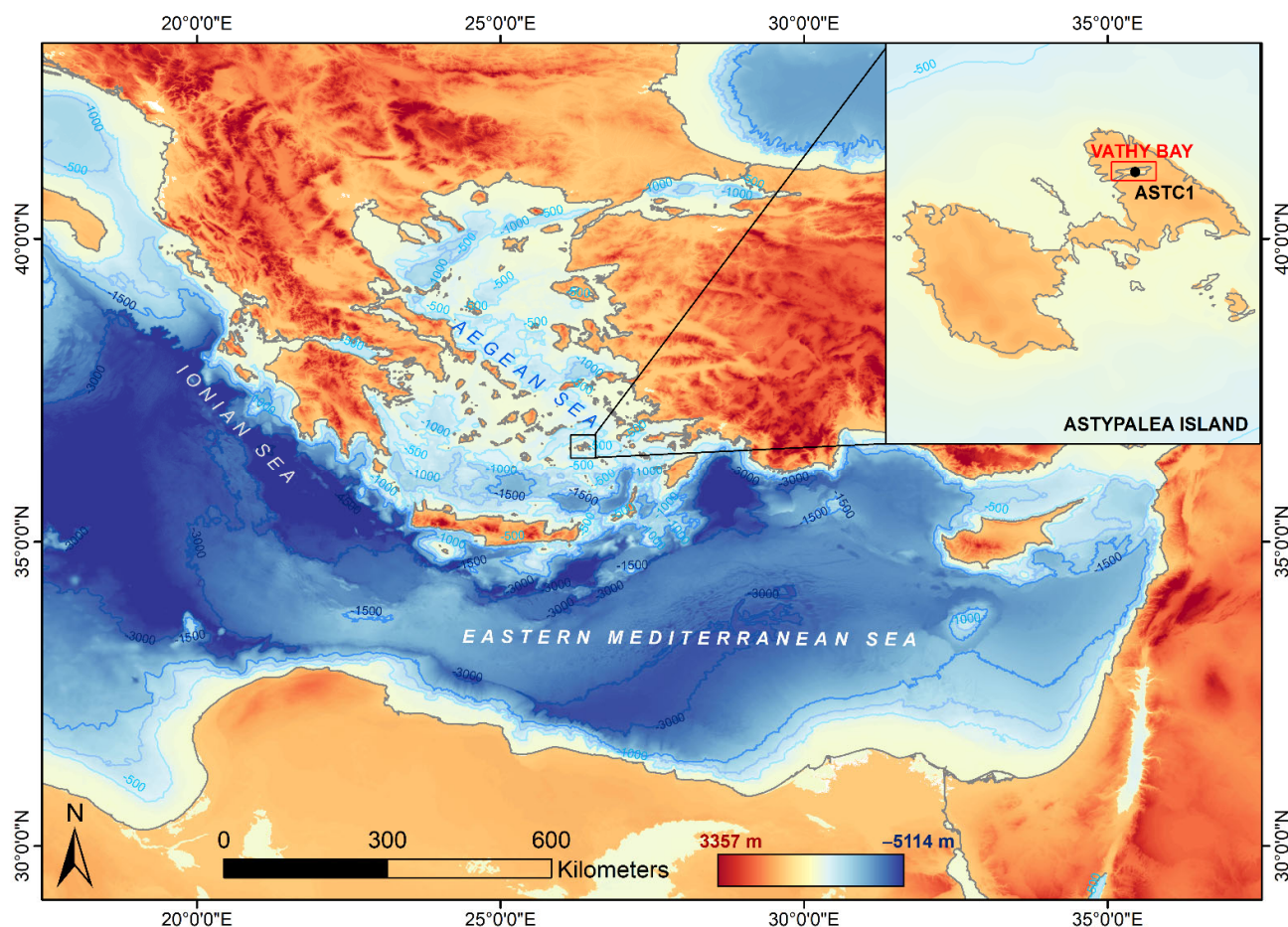


Figure 1. Map of the Eastern Mediterranean region, the location of the study site, and sediment core ASTC1. The bathymetric data were obtained from GEBCO (<https://download.gebco.net> (accessed on 15 January 2021)).

Regional Setting

The northeastern Mediterranean margin, represented by the Aegean Sea, is subdivided into two basins with different hydrographic characteristics [41]: the north and south Aegean. Within the Aegean, the Eastern Mediterranean Deep Water mass forms [42,43]. The study region is located within an N-S gradient from subhumid to arid climate conditions. In the north, river systems from surrounding landmasses, as well as the Black Sea region, impact circulation. In the south, water masses exchange with the EM through the Cretan straits. The south Aegean basin is considered a typical oceanic margin environment, lacking large terrigenous (fluvial) supplies [44]. The documented productivity rates within the euphotic zone are very low according to measurements at 200 m water depth [45], and the sediments are poor in organic carbon, with a mean value of around 0.34% [46]. The Aegean Sea contains highly saline water, with an average value of 39.2‰ and average temperatures of 16 °C in winter and 25 °C in summer.

Eustatic sea-level fluctuations, along with complex tectonics, have dominated the sedimentary processes and the palaeogeographical evolution of the Aegean region [12,47–50], with almost 50–60% of the present Aegean Sea bottom being exposed during the Last Glacial Maximum [51]. Our study area (Vathy bay) is in NE Astypalea, an island just above the Aegean volcanic arc and forms the southeastern margin of the Santorini-Amorgos Shear Zone, which experienced general uplift during the Quaternary and possibly before [52,53]. Beachrock formations, notches, and archaeological sites across the Aegean Sea coasts have been related to episodic coastal uplift and/or subsidence events during the Holocene [29].

The Vathy bay is 2 km long and 0.5 km wide, covering an area of 0.8 km². The maximum water depth is 10 m. The bay has a flat floor, and it is semi-isolated from the south Aegean Sea by a narrow and shallow strait/channel of 1 km length and 150 m width and a 4.7 m deep sill (Figure 2). Maximum temperature in July is between 25.8 and 26.8 °C and salinity ranges between 38.6 and 38.8 psu. The bedrock is composed of Upper Cretaceous limestones, scree, and Quaternary coastal deposits. The Vathy bay is surrounded by hills that provide some shelter from strong winds and waves. No evidence of Holocene fluvial input is known. Nowadays, the bay serves as a port, as it provides protection against wind and high waves. The island is sparsely populated but has a long and important human occupancy record dating back to 6 ka BP [38].

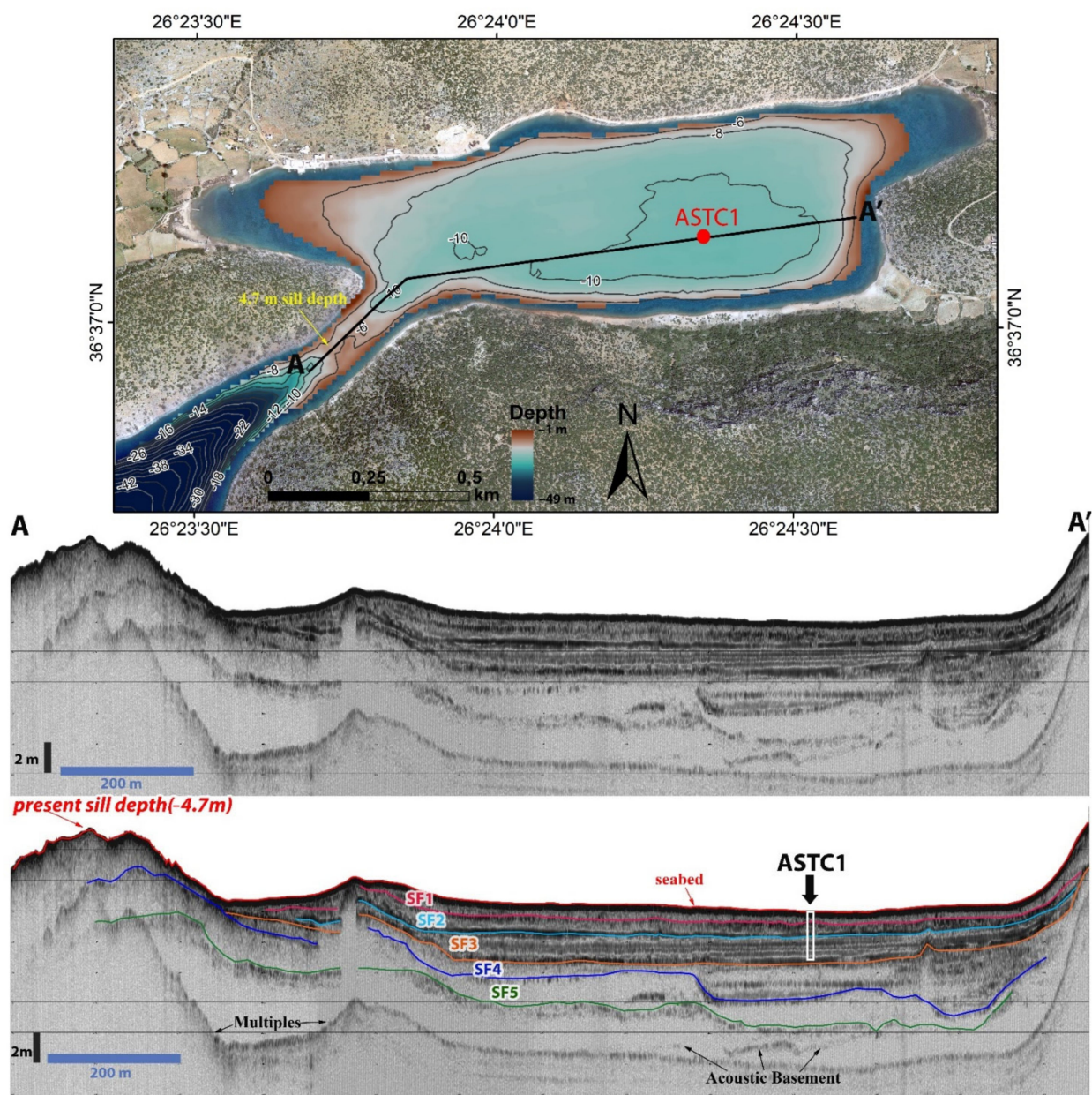


Figure 2. Bathymetric map of the gulf, showing the location of the seismic line AA' and the sediment core drilling location (top right). High-resolution seismic profile with a 5.5× vertical exaggeration of the sedimentary basin of Vathy (the uninterpreted above and the interpreted below). The interpreted profile shows the boundaries of the recognized seismic facies, the coring site, and the retrieved sedimentary units (white rectangle).

2. Materials and Methods

2.1. High-Resolution Seismic Data

High-resolution seismic data were obtained from the Vathy bay in two phases, in July 2016 and July 2018, with a research vessel specially modified to meet the marine geophysical survey needs. During the first phase, a chirp-type subbottom profiling system with 5–10 cm resolution was used, and a dense network of seismic lines was produced to obtain seismic stratigraphy. The retrieved data helped us reconstruct the seismic stratigraphy of the upper 10 m of sediments below the sea floor and helped to select a favorable coring location where the maximum sedimentary sequences could penetrate. In the second phase, seismic data of higher resolution (1–5 cm) were obtained with a parametric Innomar SES-2000 light plus subbottom profiler to provide more details regarding the inner structure of the sedimentary units that were also recognized in the chirp profiles. During all the phases of the survey, the exact positional data were provided by a Differential Global Positioning System (DGPS) with an accuracy of ± 1 –2 m. For this study, only the high-resolution seismic profile of the second phase (seismic transect AA', Figure S1) along the coring site was interpreted and correlated with the sediment core units (Figure 2). This profile is representative of the core site and the area bounded by the core site location and the straits of the bay.

The average pulse length of the stratigraphic sequence at the exact coring location was extracted from ISE processing software using the high-resolution seismic data acquired with the Innomar SES-2000 subbottom profiler. The traced signal resolution was 1 cm, and it was measured in μ s.

2.2. Sedimentological and Geochemical Analyses

One sediment core was retrieved from the central part of the bay in July 2018. The 3.2 m sediment core ASTC1 (lat. 36.618878°–long. 26.405795°) was obtained with a diver-operated (hammer) piston coring system at 9 m water depth.

A series of standard sedimentological and geochemical analyses were performed on ASTC1 core samples, such as grain size analysis, determination of total organic carbon (TOC) and total nitrogen (TN), sediment color (CIE-b*) (Avaatech Color Line Scan Camera), inorganic geochemistry, and stable isotopes.

Grain size determination was carried out on 108 samples, which were analyzed and classified based on Folk and Ward's (1957) nomenclature. The grain size measurements were made using a Malvern Mastersizer Hydro 2000 at the Laboratory of Sedimentology, University of Patras. Prior to measurement, bigger fragments—mainly biogenic (shells)—were removed by wet-sieving each sample at 1 phi. The sedimentological statistical parameters, such as mean, sorting, skewness, and kurtosis, were calculated using Gradistat V.4 software [54]. The carbonate fraction was not removed, so the grainsize also includes the bioclasts smaller than 1 phi.

Variations in nitrogen and organic carbon content in the ASTC1 core were measured with a Fisons NA1500 CN elemental analyzer at Earth Sciences Utrecht University. An average 10 cm sampling resolution was established for 42 samples. Prior to measurement, a series of pretreatments was made. First, the samples were freeze-dried, ground, and precisely weighed. To eliminate the carbonate fraction, the carbonates were removed through mechanical shaking of the sample with 1 M HCl (twice for 4 and 12 h) (for details, see [55]). Then they were washed 4 times with demineralized water, centrifuged, dried in the oven (3 days at 60°), and weighed again before being measured at the CN analyzer. The organic carbon content calculation was based on the equation $C_{org} = C\% \times (M2/M1)$, where C% is the result of the CN analyzer (decalcified sample), M1 is the sample weight before decalcification, and M2 is the sample weight after decalcification.

Sediment color data were retrieved with an Avaatech XRF core scanner equipped with a Color Line Scan Camera at the Royal Netherlands Institute for Sea Research (NIOZ). This system produces both visual color images (core photo scan) and color data in RGB and CIELa*b* (L, a*, b*) color space of that part of the core that is also 'seen' by the XRF. The set of reflectance data obtained from the sediment core on the visible light band is

then automatically transferred into coordinates of color in the CIE $L^*a^*b^*$ chromaticity space [56]. Here, we use only the b^* record, which is the color reflectance of the yellow to blue axis. This intact technique may provide various physical and geochemical indications in paleoenvironmental studies [57–62], especially when used in combination with other proxies. The applied resolution used here in the ASTC1 core was 0.07 mm, while the minimum cross-core area that can be defined is one pixel in size, which is less than 0.1 mm.

The inorganic geochemistry of ASTC1 was also measured with an Avaatech XRF (X-Ray Fluorescence) core scanner at the Royal Netherlands Institute for Sea Research (NIOZ). Prior to measurement, a protective film was placed at the part where the scan would take place. Core scanning was performed at 10, 30, and 50 kV with a step of 1 cm, and the system's detection limits ranged between Mg and Pb. Although this approach has semi-quantitative results, it can provide reliable records of the relative variability in downcore elemental composition.

In total, 40 sediment samples > 355 μm were qualitatively scanned for mollusk fauna, where common and dominant species were noted, as well as the occurrence of species with specific autecological traits (Table S1). Similarly, 60 sediment samples > 125 μm were scanned for benthic foraminifera species (Table S1).

The stable oxygen and carbon isotopic compositions of selected benthic microfossils were measured following the standard procedures of the Isotopes laboratory, Geosciences, Utrecht University. Due to the downcore coexistence of structured and homogenized sedimentary groups, the sampling interval applied in this study had to be adapted to the presence/absence of inner structures or the obvious transition in sediment texture. Sediment samples were extracted every 5 to 10 cm on average and were initially wet sieved with a 63 and 125 μm sieve, dried in an oven for 24 h, but due to big bioclasts occurrence, the 125 μm samples were extra dry sieved with a 355 μm sieve fraction. The microfossils measured for stable isotopes were the ones collected from >125 μm sieve fraction (>125 and <355) and were in majority well preserved and predominantly benthic with a total absence of planktonic species, so this study is focused on the variability of shallow water benthic species. A fraction above 355 μm was used for macroscopic observations. Residues contained gastropods, bivalves, some benthic foraminifera, and ostracods, as well as charophytes with thalli encrustations and gyrogonites (Figure 3). Hand-picked microfossils showing no signs of diagenetic alteration were selected under a Nikon SMZ800 electron microscope. Among the occurring species throughout the core, one infaunal and two epifaunal genera/species were selected, where the most abundant, such as *Ammonia* spp. tests (mainly *Ammonia tepida*, shallow infaunal sediment), *Quinqueloculina* spp. tests (epifaunal), and ostracods (Cypridoidea) tests (epifaunal), were selected from >125 μm fraction (plate 1) for stable isotope analyses. The 91 calcite tests were then treated twice with deionized water and ultrasound shaking before being dried in the oven. Afterwards, a specific amount of the samples (20–50 μg) and the standards (20–50 μg of IAEA and NAXOS) were weighed and flashed before being measured with an isotope ratio mass spectrometer (IRMS) with different preparation systems (gas chromatography-based Gas Bench II system) that each provide the analyte in a stream of helium gas, hence continuous flow. This analysis was conducted at the Isotopes Laboratory, Utrecht University. The standard deviation of the measured samples was better than 0.05‰ for $\delta^{13}\text{C}$ and better than 0.1‰ for $\delta^{18}\text{O}$.

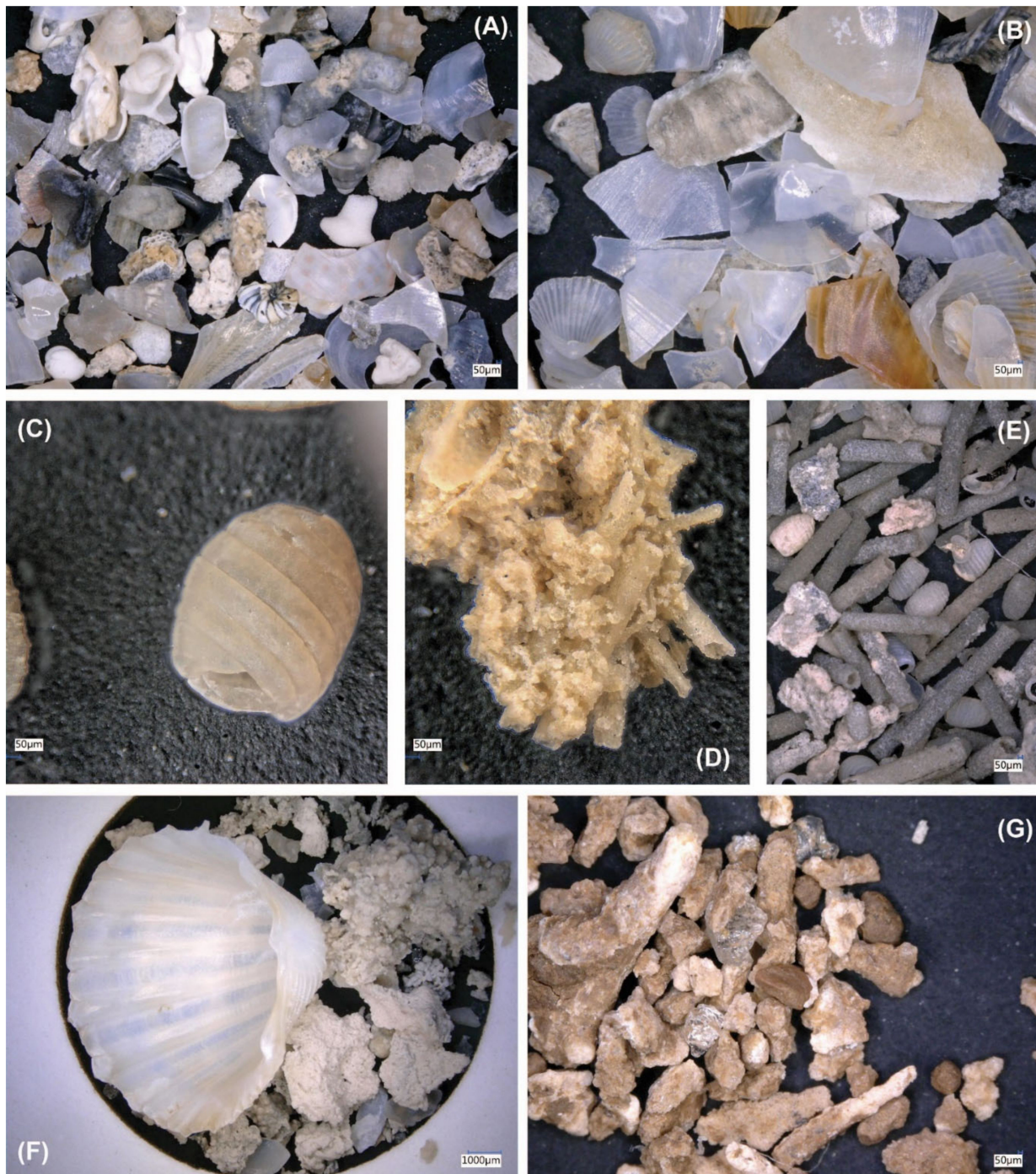


Figure 3. (A,B) mollusc fragments, (C) Gyrogonite (Charophyte oogonial cell), (D) Calcified remains of a charophyte cortex (thalli encrustation), (E) Calcified Charophyte cortex and Gyrogonites, (F) Bivalve (*Acanthocardia paucicostata*), and carbonate aggregates, (G) Clastic grains and fish bones.

The age model of core ASTC1 was based on 20 bulk $^{14}\text{C}_{\text{org}}$ measurements and one ^{14}C accelerator mass spectrometry (AMS) measurement on benthic foraminiferal tests of the species *Ammonia tepida* (Figure 4, Table 1). The ^{14}C analysis for the shell test was carried out at the Radiochronology Lab C.E.N. ULAVAL in Canada, whereas the ^{14}C dates were conducted at ETH-Zurich.

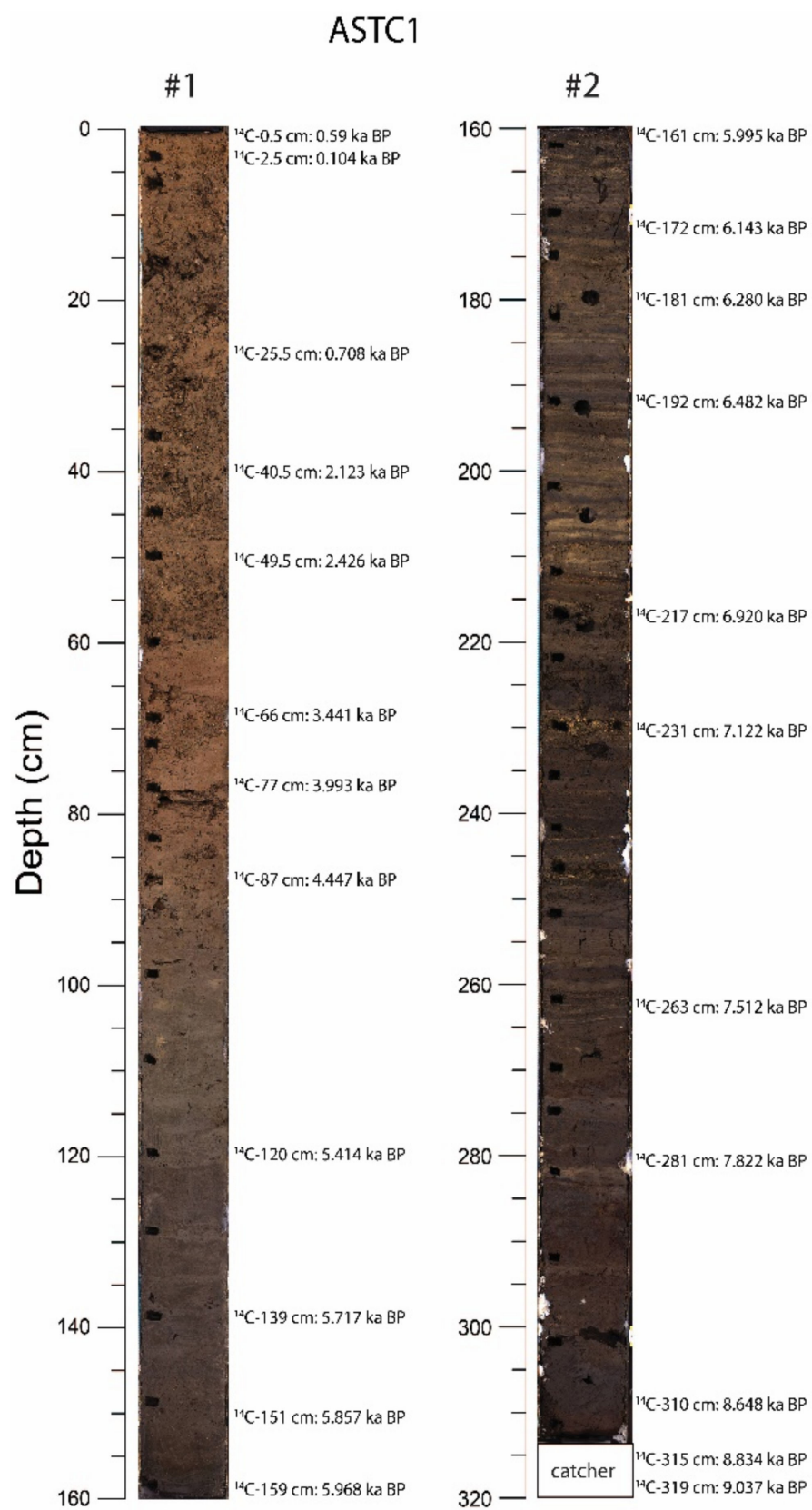


Figure 4. Calendar ^{14}C dates measured along the two sections of the ASTC1 sediment core.

Table 1. The 14C data used to construct the Age Model.

Depth (cm)	¹⁴ C Age (yr B.P.)			Calendar Age (Cal yr BP)			Material	Lab Code
0.5	623	±	65	59	±	322	Bulk sediment	BCd1
2.5	418	±	65	104	±	350	Bulk sediment	BCd2
25	1206	±	51	708	±	750	Bulk sediment	BCd3
40.5	3105	±	72	2123	±	1169	Bulk sediment	BCd4
49	2417	±	53	2426	±	1083	Bulk sediment	BCd6
66	3365	±	56	3441	±	924	Bulk sediment	BCd7
77	4185	±	56	3993	±	629	Bulk sediment	BCd9
87	4663	±	57	4447	±	638	Bulk sediment	BCd12
120	5584	±	59	5414	±	614	Bulk sediment	BCd13
139	5810	±	60	5717	±	405	Bulk sediment	BCd16
151	5555	±	60	5857	±	344	Bulk sediment	BCd17
159	5930	±	60	5968	±	309	<i>Ammonia</i> spp.	AMSC14
161	5789	±	60	5995	±	309	Bulk sediment	BCd18
172	5881	±	58	6143	±	310	Bulk sediment	BCd19
181	6047	±	59	6280	±	322	Bulk sediment	BCd20
192	6352	±	84	6482	±	374	Bulk sediment	BCd21
217	6816	±	61	6920	±	413	Bulk sediment	BCd24
231	6949	±	61	7122	±	407	Bulk sediment	BCd25
263	7073	±	62	7512	±	473	Bulk sediment	BCd27
281	7384	±	89	7822	±	540	Bulk sediment	BCd28
310	7825	±	73	8648	±	476	Bulk sediment	BCd30
315	7891	±	65	8834	±	421	Bulk sediment	BCd31
319	8305	±	66	9037	±	614	Bulk sediment	BCd32

The Marine20 and Intcal20 data sets were used for calibration [63], and a ΔR of -58 ± 85 years was adopted based on measurements of recent mollusk shell material in the Aegean basin [64]. A zero ΔR was applied to the non-water-logged samples of the sediment core.

3. Results

3.1. High-Resolution Seismic Data

The high-resolution seismic profile (AA') shows an up to 9.5 m thick sedimentary succession in the Vathy bay and a sill with a maximum depth of -4.7 m (Figure 2). The transect crosses the central part of the strait and the basin from west to east and overlies the ASTC1 core. Five main seismic facies (SF1–SF5) with different acoustic reflections were identified. Each represents a specific and distinctive depositional environment. Starting from the deeper to the shallower seismic facies, SF5 displays acoustically transparent and overlaps the acoustic basement, SF4 is semi-transparent with some weak and horizontal seismic reflectors occurring at the eastern part of the basin, SF3 is characterized by horizontal dense laminated seismic reflectors, and SF2 and SF1 show a chaotic acoustic pattern, with the last one being semi-transparent (Figure 2). The above seismic facies (SF1–SF5) show onlap termination against the slope of the acoustic basement (Figure 2). The upper three sedimentary facies (SF1–3) were cored and are the subject of this study.

3.2. Core Chronology

Bayesian age-depth modeling was performed using the R package Rbacon (v.2.3; [65]) (Figure 5). Calibrated radiocarbon dates are reported as “cal. BP” (before present, this is before 1950), according to Mook and van der Plicht (1999) [66]. The radiocarbon measurements indicate that the sediment core spans the Holocene time interval (Table 1). The core bottom is dated at 9.1 ka cal BP, whereas the core top has an age of 100 years cal BP. The sedimentation rates decreased upward from 53 to 20 cm/ka (Figure 5).

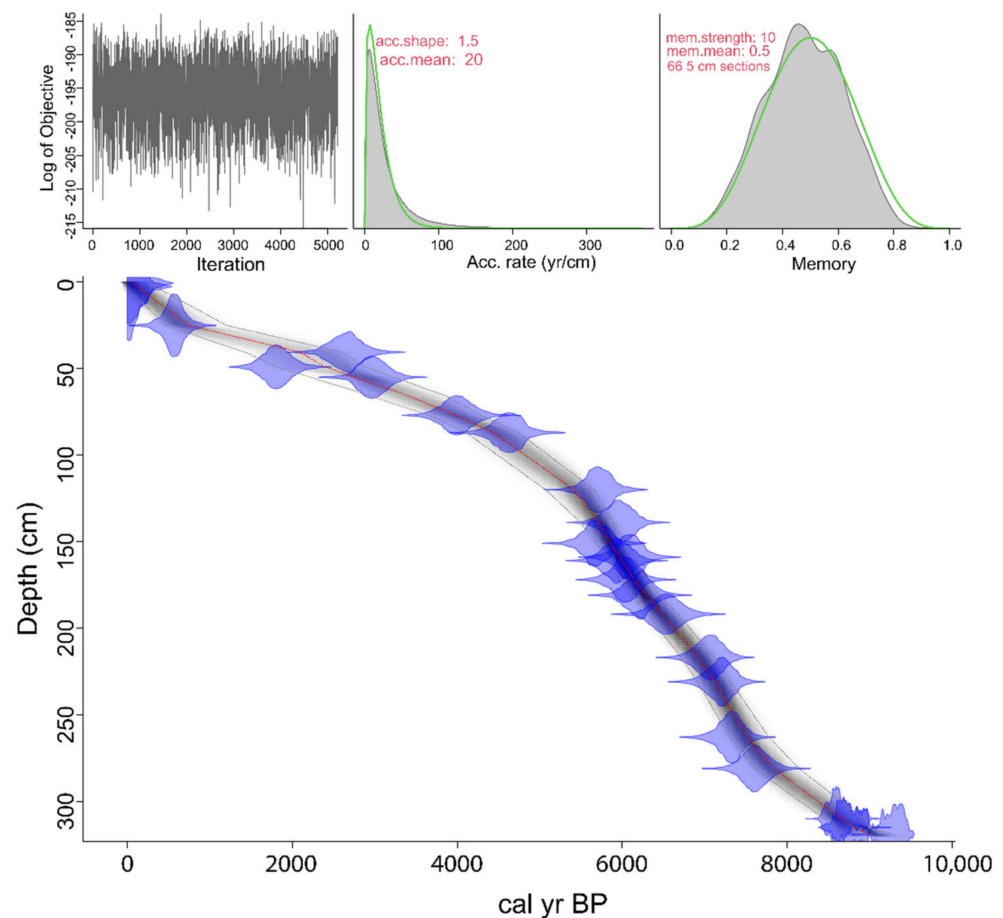


Figure 5. Bayesian age-depth model for ASTC1 sediment core in cal yr BP.

3.3. Sedimentary Units

Macroscopic observations, together with sedimentological, color reflectance, and geochemical data, suggest that the core ASTC1 consists of three main Lithological Units LU-I to LU-III (Figure 6).

The uppermost LU-I extends from a 0 to 80 cm core depth, and it comprises grayish brown to very dark grayish brown sandy mud. Within LU-I, the Fe values decline upwards, while the Ca values and the b^* record are in general high. Microscopic observations revealed the frequent presence of glass shards in the sediments of this unit. Based on the proposed age model, the LU-I spans the time interval between 4.1 ka BP and the present.

LU-II extends from 80 to 160 cm core depth, and it comprises very dark greenish gray and very fine silt to sandy mud. The base of LU-II is characterized by low values of Ca and b^* record, which mark the transition between this unit and the underlying LU-III. The values of Ca increase toward the top of the unit, while the values of Fe show an opposite trend. The timing of the deposition of unit II is estimated to be between 6 and 4.1 ka BP.

LU-III extends from the base of the core (320 cm) up to 160 cm, and it comprises a very fine to silt grain size of dark olive brown sediments. LU-III is characterized by a laminated pattern, in contrast to the more homogeneous upper and middle LU-I and LU-II. In addition, frequent short-scale variability in the values of Ca, Fe, and b^* records is observed within LU-III. The base of this unit is estimated at 9.1 ka BP.

The downcore variations in the above-mentioned proxies (grain size, values of Ca and Fe, and values of b^* record) were compared to the pulse length variation retrieved at the core site. An uncertainty of 1–5 cm is implemented by the seismic profile and the extracted pulse length according to the instrument's specifications; thus, the correlation to the sediment core units is not linear. The comparison showed that lithological units I to III correlate well with seismic facies 1 to 3, respectively, on the seismic profile (Figure 6). The

higher amplitude (large pulse length) recorded in SF1 most probably corresponds to the higher density of the sediments of LU-I. In contrast, the fine-grained sediments and the low densities in LU-III correspond to the low pulse length recorded in SF3.

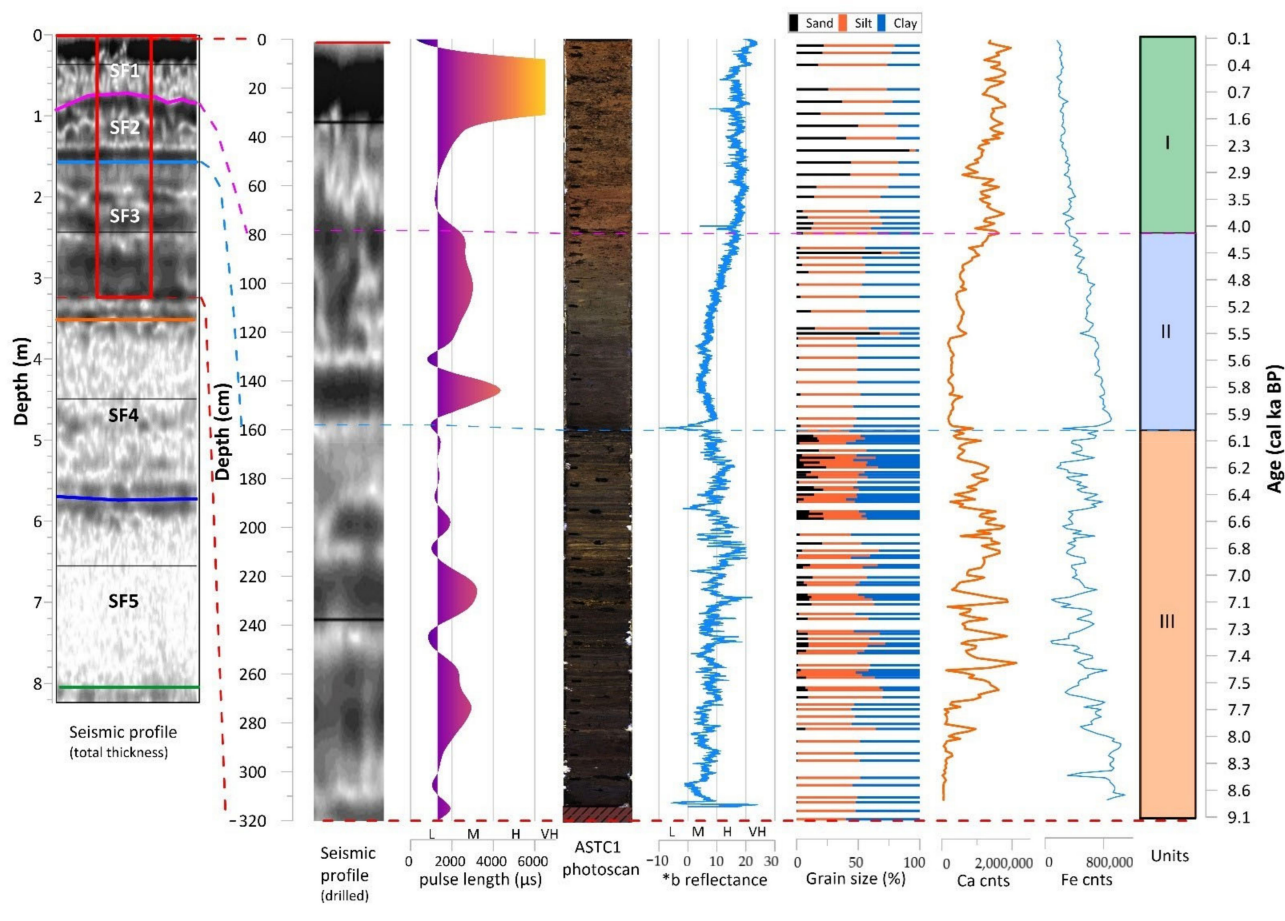


Figure 6. Correlation diagram between seismic (left) and lithostratigraphic units of ASTC1 sediment core (right). The seismic profile (total thickness) includes the core position and the different seismic facies, SF1–SF5, based on the pulse length. The lithological units are defined on the downcore *b color reflectance record, the grainsize, Ca, and Fe XRF counts. The calendar ages of the sediment core obtained in this study have been assigned to the depth axis.

3.4. Carbonate Precipitates

To evaluate the types of carbonate precipitation at the core site, the variations of the Sr/Ca and Mg/Ca ratios were examined. In shallow water marine carbonates, a high Sr/Ca ratio often represents the occurrence of aragonite [67,68]. High-Mg calcite and aragonite content is usually found in sediments lying under oversaturated water columns, such as in shallow water depth basins and/or at low latitudes [67,69].

In the ASTC1 core, the downcore variations of these ratios revealed two different carbonate mineral precipitates (Sr-rich and Mg-rich), and their dominance in specific intervals allowed for a further distinction of the lithological units into subunits (Figure 7). Units III and II were divided into subunits IIIA–IIIC and IIA–IIB, respectively. The highest Mg/Ca values are recorded in subunits IIIC (8–9.1 ka cal BP) and IIB (5.4–6 ka cal BP), while the highest Sr/Ca values are recorded in IIIA (6–7.3 ka cal BP) and IIIC (8–9.1 ka cal BP). Although the two carbonate precipitates occur individually, they co-occur in subunit IIIC, presenting a mixed carbonate precipitate pattern. On the other hand, the high Sr/Ca ratio in IIIA suggests that the water conditions were in favor of aragonite formation in the Vathy basin between 7.3 and 6 ka cal BP, possibly in the presence of discrete concretions (white laminae) (Figure 7). Notably, samples taken from IIIB and IIB, which correspond

to low and zero values of both Sr/Ca and Mg/Ca, contain abundant calcified remains of charophytes, such as cortex and thalli encrustations and gyrogonites (Figure 3c–e). In closed or semi-closed water bodies, precipitation of high-Mg calcites (high values of Mg/Ca [70]) and/or aragonites (high values of Sr/Ca [71]) could be of inorganic origin associated with increases in salinity under enhanced evaporation [16,35,70] and/or of biogenic and biological processes associated with algal blooms and removal of CO₂ [72,73].

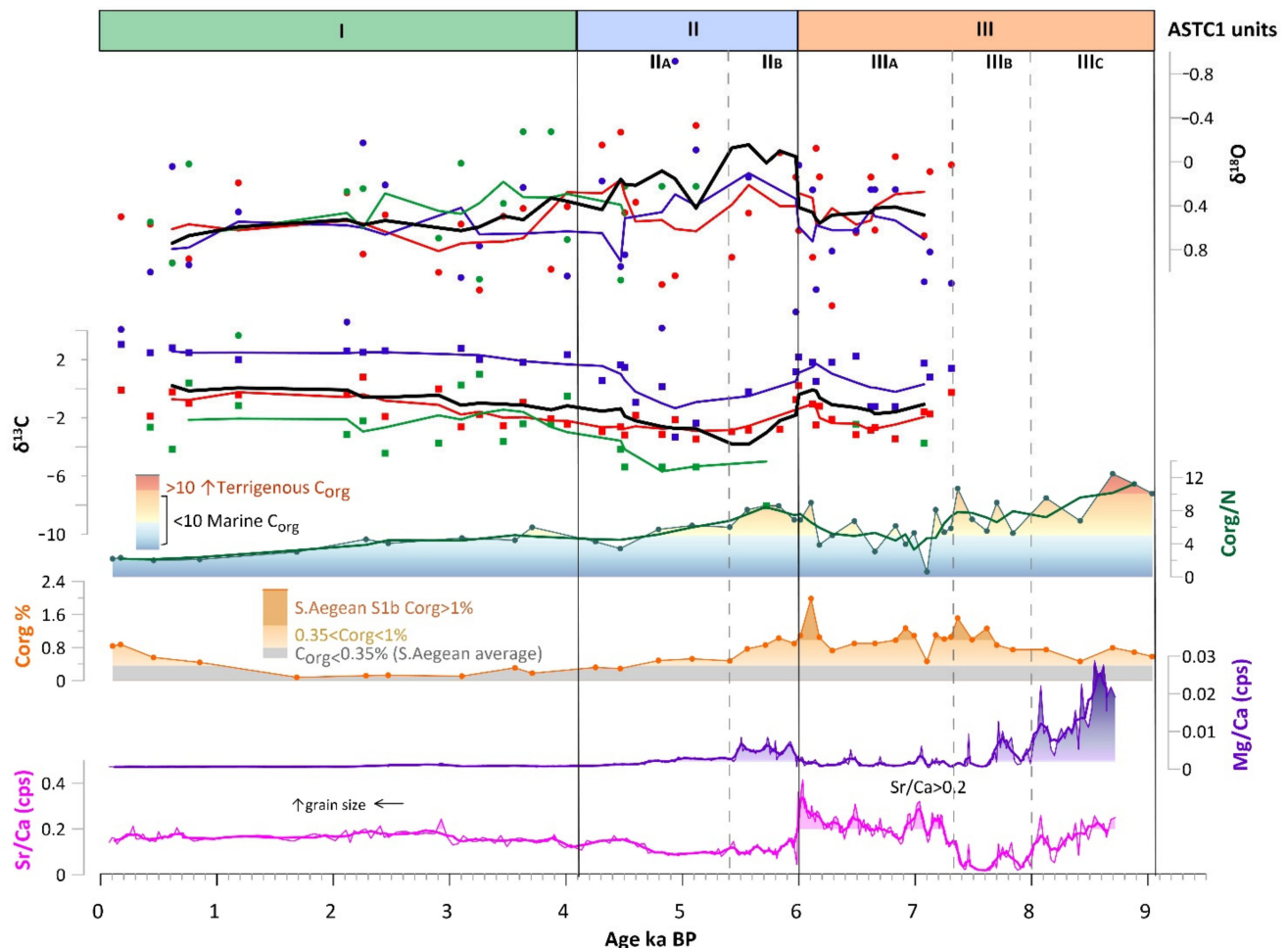


Figure 7. Synthetic plot of ASTC1 sediment core proxy record. From bottom to top: Sr/Ca (cps) and Mg/Ca (cps) geochemical ratios, total organic carbon content (%TOC) and TOC/TN (%), stable isotopes ($\delta^{13}\text{C}$ and $\delta^{18}\text{O}$), the chronologically adjusted lithological units of ASTC1, and their boundaries marked with the dashed gray line. Red color refers to *Ammonia* spp., green to ostracods, and purple to *Quinqueloculina* spp. Dots represent the absolute values of $\delta^{13}\text{C}$ and $\delta^{18}\text{O}$ whereas the colored lines refer to the 5-point running average. The black line refers to the 5-point running average of the mean $\delta^{13}\text{C}$ and mean $\delta^{18}\text{O}$ values. Three point running averages (thick line) were also calculated for Mg/Ca, Sr/Ca, Corg and Corg/N.

3.5. Organic Carbon Accumulation and Source

The Organic Carbon (C_{org}) content varies between 0.1–2% in total and follows a general upward decreasing trend throughout ASTC1. Enriched C_{org} ($>0.5\%$) values have been recorded within unit III and subunit IIB (9.1 to 5.4 ka BP), and upper unit I (0.8 ka BP to present) (Figure 7). The highest C_{org} values were observed at around 6.1, 6.9, and from 7.6 to 7.4 ka BP.

C_{org}/N ratio varies from 0.6 to 12.4 throughout the ASTC1 record, suggesting a mixed marine/terrestrial type of organic matter [74] for the bigger part of the studied interval

(Figure 7). The highest C_{org}/N values (>10) occur in subunits IIIC, IIIB, and IIB, suggesting a terrestrial organic supply [74,75] for these intervals (9.1–7.3 and 6.1–5.4 ka BP).

3.6. Mollusks and Foraminifera

Observations made on the mollusk and benthic foraminifera of core ASTC1 are provided in Table S1. LU-I contains diverse mollusk fauna in the upper part (1–50 cm) and intermediate-low diverse and less abundant marine fauna in the lower part (50–75 cm). The mollusk faunas in this unit are dominated by *Varicorbula gibba*, *Nucula nucleus*, *Acanthocardia paucicostata*, *Parvicardium exiguum*, and smooth Dentaliidae, indicative of a shallow marine seafloor with high organic content and potentially (seasonal) hypoxic conditions [76]. *Bittium reticulatum*, *Rissoa parva* s.l., and *R. membranacea* s.l. commonly occur in the upper part (typically but not exclusively suggesting subaqueous vegetation), while the abundance of *Abra alba* s.l. in the lower part of LU-I indicates fine-grained soft bottoms [77]. Benthic foraminifera assemblages are dominated by epifauna and epiphytic species (*Quinqueloculina* spp., *Peneroplis* spp., *Rosalina* spp., *Planorbulina* spp. [78–81], and infauna species (*Ammonia* spp., *Melonis* spp.) that favor high organic matter and tolerate dysoxia [79,82]. The lower part of unit I, an increase in infauna/epifauna ratio is observed suggesting a reduction of oxygen conditions in the bottom waters [83].

Common mollusk species in subunit IIA include *Rissoa parva* s.l., *Parvicardium exiguum*, and *Acanthocardia paucicostata*. The upper part of this subunit (80–90 cm) contains a low-intermediate diverse fauna dominated by *Varicorbula gibba*, while other species, such as *Bittium reticulatum*, *Abra alba* s.l., *Nucula nucleus*, and *Pussilina inconspicua* s.l., also occur. The faunal composition of the lower subunit IIA (91–110 cm) is slightly variable and dominated by *Abra alba*, while some *Cerastoderma glaucum* s.l. occurs at the base. Subunit IIB contains faunas entirely dominated by *Cerastoderma glaucum* s.l., and a few *Abra alba* fragments also occur. These species have been found in the littoral zones of carbonate-rich freshwater or brackish shallow water lakes ([84] and references therein). *Cerastoderma glaucum*-dominated populations are often found in euryhaline or in mesohaline settings, and in particular, they can dominate in lagoons, saline lakes, and estuaries [1]. Within this subunit at 139.5 cm depth, a layer consisting of Characeae occurs that lacks marine shells (Figure 3c–e). Benthic foraminifera assemblages also present low abundance and low diversity in subunit II. Dominant taxa are *Ammonia* spp. and *Quinqueloculina* spp., while *Miliolinella* spp., *Melonis* spp., and *Triloculina* spp. are also present. These genera have been linked to inner shelf environments, from brackish to hypersaline lagoons ([85] and references therein).

Some mollusk species were found only in upper unit III (subunit IIIA), mainly dominated by *Varicorbula gibba*, and some *Cerastoderma glaucum* s.l., occurring at 174.5 and 231.5 cm. The presence of other mollusk faunas is rare, mainly found at the top of IIIA (161.5 cm), including the species *Rissoa parva* s.l., *R. membranacea* s.l., *Nucula nucleus*, *Bittium reticulatum*, and *Acanthocardia paucicostata*, which were also present at the younger units of ASTC1 core. Benthic foraminifera specimens were observed only in IIIA, and when they were present, they usually belonged to the genera of *Ammonia* spp., *Quinqueloculina* spp., *Melonis* spp., *Haynesina* spp., and *Rosalina* spp.

Below subunit IIIA, no fossils were found (Figure 7) apart from very few ostracods and charophytes (oospores and gyrogonites) in subunit IIIB and upper IIIC (at 270, 285, and 295 cm depth).

3.7. Stable Isotopes

The stable isotope data of *Ammonia* spp., *Quinqueloculina* spp., and ostracods comprise the past 7.3 ka BP of the ASTC1 sediment core (Figure 7). There appears to be relatively large variability between the individual samples in both $\delta^{13}C$ and $\delta^{18}O$ values, which may point to a large seasonal imprint on the picked and analyzed specimens. To derive a clearer picture of the isotopic trends within the Vathy bay over the past 7.3 ka, we applied a five-point running average. Evidently, the $\delta^{13}C$ and $\delta^{18}O$ trends derived from this approach

show that the individual microfauna followed a highly comparable (similar) pattern during the Holocene (Figure 7).

Unit I and subunit IIIA are characterized by mean $\delta^{13}\text{C}$ ratios of -2 to 0‰ and become more negative downwards in unit II, especially at its basal subunit IIB (-4 to -2‰) (Figure 7). Similarly, the average $\delta^{18}\text{O}$ ratios of unit I and subunit IIIA are generally high (i.e., an average value of 0.4 to 0.8‰) compared to those of unit II (i.e., ranging between -0.1 to 0.2‰). The $\delta^{13}\text{C}$ and $\delta^{18}\text{O}$ ratios became higher toward the top of the core (Figure 7).

Offsets in the isotopic signal between *Ammonia* spp. and *Quinqueloculina* spp. have been attributed to a combination of vital effects and seasonal differences in the timing of shell calcification [86–89]. Scourse et al. (2004) [86] showed that *Ammonia batavus* calcifies during the same period as *Quinqueloculina seminulum* (September) when stratified conditions occur in a continental shelf environment. When conditions change to mixed conditions, *Ammonia batavus* calcifies during spring or early summer. Epifaunal taxa are commonly close to the isotopic signature of bottom water $\delta^{13}\text{C}$ DIC whereas infaunal taxa bear a strong pore water signal, which is marked by depleted $\delta^{13}\text{C}$ [90–100].

4. Discussion

4.1. Palaeoenvironmental Evolution

Combining all proxies enables the documentation of several phases within the depositional system and its biota and the identification of the driving mechanism of environmental change. More specifically, the sediments of the lower LU-III represent a transition from a terrestrial to a water-logged environment. The absence of any shells in subunit IIIC (9.1 to 8 cal ka BP) indicates the development of a terrestrial environment isolated from the open sea (Figure 8). This is further supported by terrestrial organic matter with high $\text{C}_{\text{org}}/\text{N}$ values (Figure 7). On the seismic profiles (Figure 2), the strong reflections of uneven surfaces recorded at the base of the SF3 provide evidence for the deposition of high-density, subaerial exposed, and eroded sediments, along at least an area between the core site and the sill of the bay (Figure 2).

In the overlying seismic phases SF1–SF3, the acoustic signal amplitude decreases (Figure 6). Internal reflections are horizontal, suggesting subaquatic sediment deposition. This change correlates with a shift in the biological content occurring in the sediment samples of subunit IIIB. Episodic presence of Charophyta (Figure 3) in the examined samples from subunit IIIB, indicative of freshwater conditions [97], implies the establishment of an ephemeral pond/lake, at least at the core site between 8 and 7.3 cal ka BP. Within this interval, the organic carbon content is elevated, and thus may indicate low rates of organic matter metabolism under intense water stratification and/or high rates of organic matter flux. High organic matter intervals mostly coincide with high $\text{C}_{\text{org}}/\text{N}$ ratios, suggesting an increase in terrestrial organic supply. In addition, minor fluctuations of Sr/Ca and Mg/Ca ratios coincide with high C_{org} content suggesting that within this interval the precipitation of Sr-rich and Mg-rich calcites in the sediments of the pond/lake was favored at times of anoxic bottom water conditions or enhanced lake productivity ([98] and references within).

These short-scale environmental changes may be linked to minor climatic fluctuations in the area. According to the proposed age model, it is estimated that subunit IIIB was deposited between 8 and 7.3 cal ka BP, an interval where previous studies have shown EM humidity fluctuations (i.e., N. Aegean Sea [99]; Lebanon, Jeita Cave [100]) within a general warm period [2]. These climatic conditions contributed to an oceanographic regime that led to the deposition of the second sub-sapropel S1b in the EM (7.9 – 6.5 ka BP [6]). Increased precipitation at the Vathy bay area likely enabled the establishment of an ephemeral pond/lake, where the high temperature would have enhanced water stratification, oxygen deprivation, and organic matter accumulation.

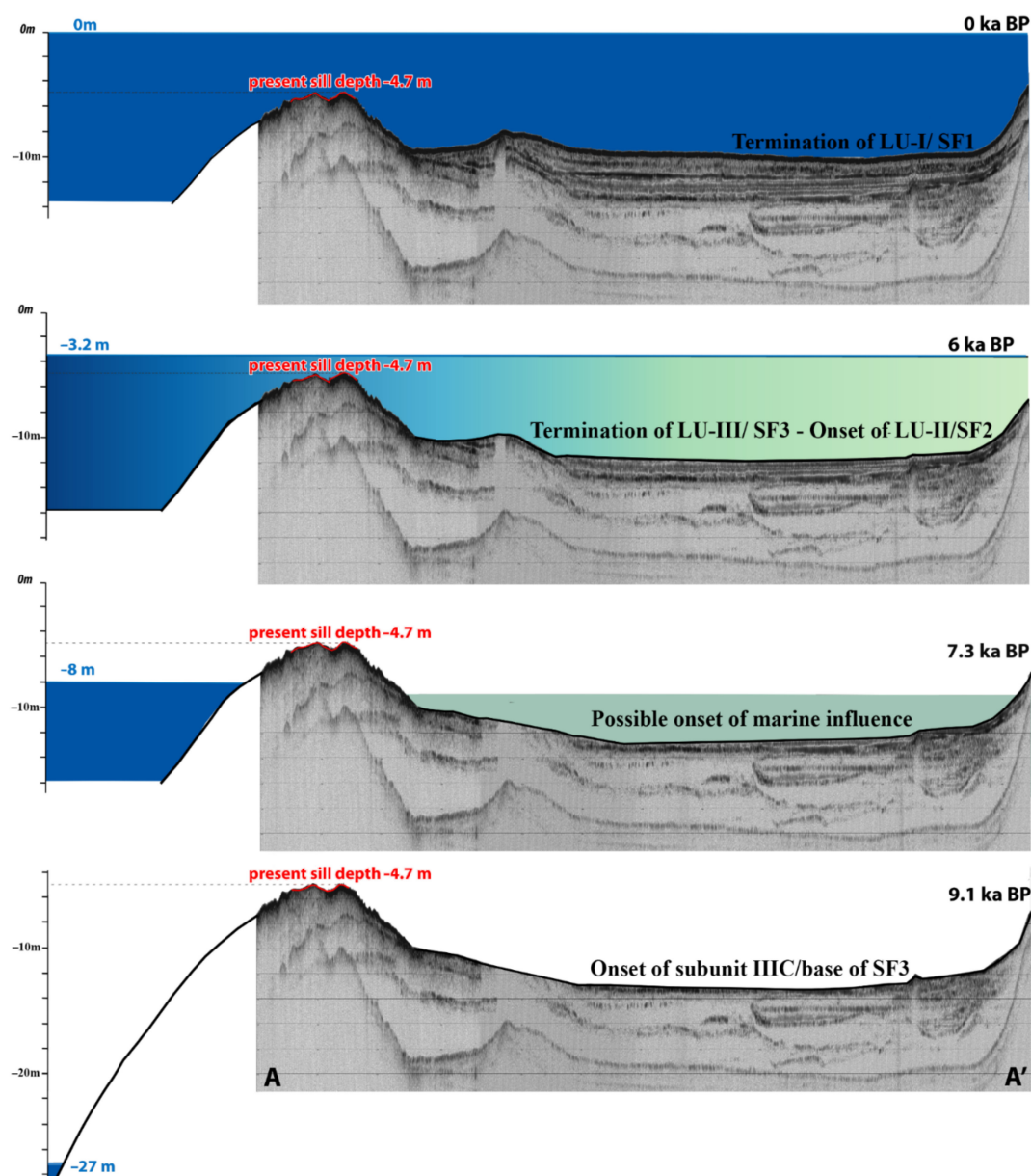


Figure 8. Reconstruction of the different basin phases within the 9.1 ka BP time interval. Each phase represents the lithological unit of the ASTC1 sediment core. Global mean sea level, following Lambeck et al. [23].

During the successive deposition of subunit IIIA, organic matter accumulation increased (Figure 7), and marine/euryhaline shells occurred at 7.3 ka BP (Table S1), indicating that marine conditions had been established.

The mollusk and benthic assemblages are of low abundance and low diversity, and the laminated character of subunit IIIA indicates the prevalence of low oxygen conditions on the seafloor. In addition, high values of Sr/Ca ratio together with heavier $\delta^{18}\text{O}$ values point to the establishment of high salinity waters [101]. Within this interval (7.3–6.2 ka), arid conditions have been reported in the Anatolia region [2,100,102]. The studied area also experienced aridity during this period, with the high evaporation rates inducing the precipitation of aragonite, pointed out by the high Sr/Ca ratio, in this newly established marine environment ([35] and references therein).

This contrasts with the findings of the overlying subunit IIB (6–5.4 ka BP), where the mollusk and the benthic foraminifera assemblages suggest the establishment of a lagoonal

environment ([85,103] and references within). The depletion in the $\delta^{18}\text{O}$ values and the cease in the precipitation of aragonite (low values of Sr/Ca ratio) imply a reduction in salinity in the waters [101]. Previous studies have shown an increase in humidity and a decrease in temperature during this interval [2,100]. Thus, an increase in the freshwater supply together with low temperature, along with the elevated increase in the water depth, may have altered the former hypersaline marsh into a lagoon.

The continuous sea level rise led gradually to the dominance of marine waters over low salinity waters. This signal started to be observed within subunit IIA. There, the increase in the abundance and diversity of mollusk and benthic foraminifera assemblages, together with an enrichment in the stable oxygen isotope values, suggest the prevalence of more saline waters and more oxygenated seafloors. In addition, from IIA onwards, the low values of C_{org}/N ratio suggest that the organic matter is of marine origin [26]. As for subunit IIA and onwards, the seafloor environmental conditions do not present any influence by the sea level changes but rather appear to be regulated mainly by the internal oceanographic conditions developed in the bay. The dominance of benthic foraminifera and mollusk species that tolerate dysoxia and/or favor high organic matter contents suggests that stressful bottom conditions prevailed in the Vathy bay from 5.4 to 4.1 ka cal BP, corresponding to the deposition of subunit IIA and the lower part of unit I. An improvement in the bottom water oxygen concentration is suggested for the last 4 ka in the bay, based on the dominance of microfauna sensitive to oxygen availability. The high water depth (−0.5 m) reached at 2.5 ka BP [23] may have enhanced the water circulation in the bay, bringing fresh oxygenated waters from the open sea, and thus improving the seafloor conditions.

4.2. Global Sea Level and Flooding of the Bay

According to the proposed age model of the present study, subunits IIIC and IIIB were deposited from 9.1 to 7.3 ka BP. Within this interval, the models for the global eustatic sea level change show that the sea level rose from −27 m (at 9.1 ka BP) to −8 m (at 7.3 ka) [13,23]. Such sea levels are well placed below the present depth of the sill (−4.7 m) suggesting that the bay (and the core site) was isolated from the open sea for the total period of the depositions of IIIC and IIIB. This observation further supports the nature of the depositional environments attributed previously to subunits IIIC and IIIB (land and pond/lake, respectively). On the contrary, the 4 m difference between the global mean sea level stand and the depth of the sill at the time of the onset of subunit IIIA (7.3 ka) cannot explain the inundation of the sea according to the eustatic sea-level curve as far as the core site.

To explain this earlier than expected sea inundation in the bay, regional and/or local scale factors should be further investigated. Onlap geometries of the upper sedimentary sequences recorded in the inner basin could indicate differences in the rate of sediment supply and/or differences between the rate of sea-level fluctuations and the rate of local tectonic-induced vertical displacements [104]. For instance, tectonic studies have shown that the entire central Aegean region experienced a general uplift during the Quaternary [52,53]. However, more specific archaeological data, beach rock formations, and rocky notches from the south Aegean region and the Minor Asia coasts have provided evidence of both subsidence and uplift events of variable magnitude during the Holocene [13,14,27,40,44,51,105] linked to intense regional tectonic activity [105]. Although an overall specific trend (subsidence or uplift) is not provided for the SE Aegean Sea, and for the Astypalea area in particular, their recording indicates that they may produce relative sea level changes that may be incompatible with the already predicted eustatic—isostatic ones [13,23,106]. Following this approach, the scenario of the relative sea level changes of episodic or summarized over time character seems to be plausible and responsible for the earlier-than-expected marine flooding of the bay.

An alternative scenario that could explain the earlier-than-expected flooding of the Vathy basin may involve the possibility of a sea entrance linked with a tsunami. Although

the island is situated in an area where earthquakes have triggered tsunamis in the past [107], the steady presence and the increasing abundance of all taxa associated with saline waters, from 7.3 ka BP onwards, suggest that a marine inundation related to a tsunami should be most likely excluded.

Finally, a likely explanation is that the massive carbonate formations (limestones) on the island and the associated karstification may have induced the prevalence of sea in the bay, independent of sea levels. This karstification, in turn, could have formatted underground channels connecting the bay to the open sea, thus establishing a marine lake environment in the bay between 7.3 and 6.8 ka BP. Such seawater seepage through karstified sill contributes to the establishment of brackish marine lake conditions, as shown by other cases on the Dalmatic coasts [16]. The large variability in the C_{org}/N ratio in IIIA suggests that the basin's connectivity to the Aegean may still have been vulnerable to small changes in sea level and the freshening of the basin, either by being influenced by karstic communication or by higher precipitation.

4.3. Climate Evolution and Human Inhabitation

Sapropel S1 is the most well-documented deposition in the marine sediments of the eastern Mediterranean during the Holocene, related to climatic change [1,5]. In our records, the deposition of S1 coincides over time with LU III, dated between 9.1 and 6.0 ka BP. LU III is rich in organic carbon content (C_{org}) (~1.2–2%) and favors Sr-rich (authigenic) carbonate formation (Sr/Ca) (Figure 7). It is striking that the timing of subunits IIIA and IIIB corresponds to the second part of the Sapropel S1, the S1b, which was deposited between 7.8 and 6.1, on average, in the EM, while subunit IIIC should coincide with the upper part of the S1a and the short interruption that was found in the S1 at around ~8.2–7.9 ka BP [6,108,109]. LU IIIA and LU IIIB are characterized by a laminated pattern. Such parallel laminations are usually recognized in lacustrine or semi-enclosed water basins, where depositional and hydrodynamic processes favor their formation and preservation [35,110,111] and may be linked to climatic variability. LU III is rich in organic carbon content (C_{org}) (~1.2–2%) and favors Sr-rich (authigenic) carbonate formation (Sr/Ca) (Figure 7). The shallowest occurrence of sapropel layer S1 in EM sediment cores is found in water depths of ~120 m [112], apart from a core (GM2) in the Marmara Sea, where sapropel S1 was found at a water depth as shallow as 37 m [113]. Since the laminated section of ASTC1 was formed when there was no full marine connection, it is highly unlikely that this interval represents an even shallower expression of sapropel S1 in the EM. Instead, due to its timing, it may have been plausible that besides changes in global mean sea level, regional and circum-Mediterranean climatic conditions [64,114,115] may have played a pivotal role in the formation and preservation of this laminated feature.

In this light, the gradual increase in $\delta^{18}O_{mean}$ values from the upper subunit IIA until the top of LU-I may prelude either the gradual increase of marine water into the Vathy basin (Figures 7 and 8) or the gradual decrease in precipitation in the Eastern Mediterranean [116,117] or increased aridity in the Aegean [1,115]. The latter has been suggested by several planktonic $\delta^{18}O$ records of EM [118–120]. At present, however, we cannot distinguish between what part of the $\delta^{18}O_{mean}$ signal is related to this aridification trend in the region and what relates to the relatively larger marine influence within the bay throughout the Holocene. The evolution of the landscape conditions from hinterland to brackish and to coastal environments seems to be conducive to the human settlement in the area. Archeological investigations have shown that settlements of human occupation in the Vathy region go back to at least the Late Neolithic Period at 6 ka BP [38]. It is an interval that is generally characterized by relative sea-level stability and human expansion into coastal areas [121,122]. According to several studies, coastal areas characterized by fertile soils and constant freshwater supply, as are the deltaic environments, were more conducive to human settlement and the development of societies and trades along the coasts [122]. Similar conditions were developed at Vathy during that period. In our records, during the Late Neolithic period, the Vathy was already connected to the Aegean Sea, though this

interval coincides with the establishment of brackish conditions related to the subunit IIA, thus contributing to the sedentarization of humans in the site.

5. Conclusions

Coastal restricted basins are sensitive recorders of both global sea level and regional-scale climate changes and thus provide a reliable archive toward their reconstruction. The examination here was based on a high-resolution seismic profile, together with sedimentological and geochemical data retrieved from a marine sediment core (ASTC1) of a semi-enclosed basin in the south Aegean Sea. The examination of the sediments included sedimentary observations and faunal, stable isotope, and geochemical analyses, while a dense grid of radiocarbon analyses led to an accurate dating for the observed paleoenvironmental changes of the bay. These changes appear to be modulated not only by the global/regional sea level rise but also by the general climatic pattern in the EM and the morphological features of the basin.

The main outcomes of our research can be summarized as follows:

- The cross-correlation of the seismic and sediment core data presents a causal link and suggests that the basin experienced three major environmental stages during the Holocene recorded as seismic facies (SF1-3) on the profiles and lithological units (LU I-III) in the sedimentary deposits.
- The transition gradually developed through several intermediate environmental stages, as shown by this study, also providing important information on the climatic pattern of the Eastern Mediterranean region. The topography of the Vathy bay forms a natural well-protected area favoring the inhabitation of prehistoric humans. Since Neolithic times, the area has also offered freshwater sources, while the establishment of a series of water bodies contributed to the further exploitation of the associated ecosystems.
- The environmental conditions changed gradually from completely isolated to the present shallow marine in the last 9.1 ka due to the post-glacial sea level rise.
- The onset of the marine influence, according to our findings, is placed at around 7.3 ka when the global mean sea level was at -8 m, ~ 3 m lower than the basin's sill. Relative arid outbreaks were pointed out within the 7.3–6 ka BP interval, which favored Sr-rich carbonate precipitation in the basin, and a general aridification or less precipitation trend as of 4.1 ka BP till present.
- Wetter conditions were instead implied for the 9.1–7.3 ka and 6–5.4 ka intervals, which coupled with the general humid conditions in the Eastern Mediterranean at those times.

Supplementary Materials: The following supporting information can be downloaded at: <https://www.mdpi.com/article/10.3390/w14223688/s1>, Table S1: Biota contained in the studied sediment samples of core ASTC1, Figure S1: Bathymetric map of the study area showing the tracklines (green) of the subbottom profilers. The red colored transect (AA') indicates the location of the profile presented in Figure 2 and investigated in the manuscript.

Author Contributions: Conceptualization, A.N., M.G. and L.J.L.; Data curation, A.N., L.J.L., M.G., F.P.W., N.H., N.G., D.C. and X.D.; Formal analysis, A.N., M.G., L.J.L., F.P.W. and N.G.; Field work, A.N., N.G., D.C., X.D., M.G. and G.P.; Methodology, A.N., M.G., L.J.L., F.P.W., N.H. and S.S.; Project administration, M.G., G.P. and A.G.V.; Supervision, M.G., L.J.L. and G.P.; Validation, N.G., L.J.L., M.G., G.P. and F.P.W.; Visualization, A.N.; Roles/Writing—original draft, A.N., L.J.L., M.G. and F.P.W.; Writing—review & editing, A.N., L.J.L., M.G., F.P.W. and N.G. All authors have read and agreed to the published version of the manuscript.

Funding: Part of this survey was funded by the State Scholarships Foundation (IKY) of Greece, with grant number 2018-050-0502-13713. The publication of this article has been financed by the Research Committee of the University of Patras.

Institutional Review Board Statement: Not applicable.

Informed Consent Statement: Not applicable.

Data Availability Statement: Experimental data are available from the corresponding author upon request.

Acknowledgments: The authors would like to thank Tobias Agterhuis for his help on sample preparation, and the technicians Arnold van Dijk and Desmond Eefting for the isotope analysis run from Utrecht University. For XRF core scanning, we would like to thank Piet van Gaever, Senior Research Assistant of NIOZ Royal Netherlands Institute for Sea Research. We are, also, thankful to Amalia Prandekou for information on benthic foraminifera and Alexandros Emmanouilidis for his help on the age model from the University of Patras. Finally, we thank the two divers Kostas and Tasos Kouvas who carried out the sediment core acquisition.

Conflicts of Interest: The authors declare no conflict of interest. The funders had no role in the design of the study; in the collection, analyses, or interpretation of data; in the writing of the manuscript; or in the decision to publish the results.

References

1. Rohling, E.J.; Mayewski, P.; Abu-Zied, R.; Casford, J.; Hayes, A. Holocene Atmosphere-Ocean Interactions: Records from Greenland and the Aegean Sea. *Clim. Dyn.* **2002**, *18*, 587–594. [\[CrossRef\]](#)
2. Rohling, E.J.; Marino, G.; Grant, K.M.; Mayewski, P.A.; Weninger, B. A Model for Archaeologically Relevant Holocene Climate Impacts in the Aegean-Levantine Region (Easternmost Mediterranean). *Quat. Sci. Rev.* **2019**, *208*, 38–53. [\[CrossRef\]](#)
3. Rossignol-Strick, M.; Nesteroff, W.; Olive, P.; Vergnaud-Grazzini, C. After the Deluge: Mediterranean Stagnation and Sapropel Formation. *Nature* **1982**, *295*, 105–110. [\[CrossRef\]](#)
4. Emeis, K.C.; Schulz, H.; Struck, U.; Rossignol-Strick, M.; Erlenkeuser, H.; Howell, M.W.; Kroon, D.; Mackensen, A.; Ishizuka, S.; Oba, T.; et al. Eastern Mediterranean Surface Water Temperatures and $\delta^{18}\text{O}$ Composition during Deposition of Sapropels in the Late Quaternary. *Paleoceanography* **2003**, *18*. [\[CrossRef\]](#)
5. Rohling, E.J.; Marino, G.; Grant, K.M. Mediterranean Climate and Oceanography, and the Periodic Development of Anoxic Events (Sapropels). *Earth-Sci. Rev.* **2015**, *143*, 62–97. [\[CrossRef\]](#)
6. Hennekam, R.; Jilbert, T.; Schnetger, B.; De Lange, G.J. Solar Forcing of Nile Discharge and Sapropel S1 Formation in the Early to Middle Holocene Eastern Mediterranean. *Paleoceanography* **2014**, *29*, 343–356. [\[CrossRef\]](#)
7. Kidd, R.B.; Cita, M.B.; Ryan, W.B.F. *Stratigraphy of Eastern Mediterranean Sapropel Sequences Recovered during DSDP Leg 42A and Their Paleoenvironmental Significance*; Government Printing Office: Washington, DC, USA, 1978; Volume 42. [\[CrossRef\]](#)
8. Shaw, H.F.; Evans, G. The Nature, Distribution and Origin of a Sapropelic Layer in Sediments of the Silicia Basin, Northeastern Mediterranean. *Mar. Geol.* **1984**, *61*, 1–12. [\[CrossRef\]](#)
9. Rohling, E.J.; Gieskes, W.W.C. Late Quaternary Changes in Mediterranean Intermediate Water Density and Formation Rate. *Paleoceanography* **1989**, *4*, 531–545. [\[CrossRef\]](#)
10. Jorissen, F.J.; Asioli, A.; Borsetti, A.M.; Capotondi, L.; de Visser, J.P.; Hilgen, F.J.; Rohling, E.J.; van der Borg, K.; Vergnaud Grazzini, C.; Zachariasse, W.J. Late Quaternary Central Mediterranean Biochronology. *Mar. Micropaleontol.* **1993**, *21*, 169–189. [\[CrossRef\]](#)
11. Rohling, E.J.; de Stigter, H.C.; Vergnaud-Grazzini, C.; Zaalberg, R. Temporary Repopulation by Low-Oxygen Tolerant Benthic Foraminifera within an Upper Pliocene Sapropel: Evidence for the Role of Oxygen Depletion in the Formation of Sapropels. *Mar. Micropaleontol.* **1993**, *22*, 207–219. [\[CrossRef\]](#)
12. Kapsimalis, V.; Drakopoulou, P.; Kapsimalis, V.; Pavlopoulos, K.; Panagiotopoulos, I.; Drakopoulou, P.; Vandarakis, D.; Sakelariou, D.; Anagnostou, C. Geoarchaeological Challenges in the Cyclades Continental Shelf (Aegean Sea). *Z. Für Geomorphol.* **2009**, *53* (Suppl. S1), 169–190. [\[CrossRef\]](#)
13. Benjamin, J.; Rovere, A.; Fontana, A.; Furlani, S.; Vacchi, M.; Inglis, R.H.; Galili, E.; Antonioli, F.; Sivan, D.; Miko, S.; et al. Late Quaternary Sea-Level Changes and Early Human Societies in the Central and Eastern Mediterranean Basin: An Interdisciplinary Review. *Quat. Int.* **2017**, *449*, 29–57. [\[CrossRef\]](#)
14. Flemming, N.C.; Harff, J.; Moura, D.; Burgess, A.; Bailey, G.N. *Submerged Landscapes of the European Continental Shelf: Quaternary Paleoenvironments*; Wiley: Hoboken, NJ, USA, 2017; ISBN 9781118922132.
15. Simaiakis, S.M.; Rijdsdijk, K.F.; Koene, E.F.M.; Norder, S.J.; Van Boxel, J.H.; Stocchi, P.; Hammoud, C.; Kougioumoutzis, K.; Georgopoulou, E.; Van Loon, E.; et al. Geographic Changes in the Aegean Sea since the Last Glacial Maximum: Postulating Biogeographic Effects of Sea-Level Rise on Islands. *Palaeogeogr. Palaeoclimatol. Palaeoecol.* **2017**, *471*, 108–119. [\[CrossRef\]](#)
16. Brunović, D.; Miko, S.; Hasan, O.; Papatheodorou, G.; Ilijanić, N.; Miserocchi, S.; Correggiari, A.; Geraga, M. Late Pleistocene and Holocene Paleoenvironmental Reconstruction of a Drowned Karst Isolation Basin (Lošinj Channel, NE Adriatic Sea). *Palaeogeogr. Palaeoclimatol. Palaeoecol.* **2020**, *544*, 109587. [\[CrossRef\]](#)
17. Geraga, M.; Tsaila-Monopolis, S.; Ioakim, C.; Papatheodorou, G.; Ferentinos, G. Evaluation of Palaeoenvironmental Changes during the Last 18,000 Years in the Myrtoon Basin, SW Aegean Sea. *Palaeogeogr. Palaeoclimatol. Palaeoecol.* **2000**, *156*, 1–17. [\[CrossRef\]](#)

18. Geraga, M.; Tsaila-Monopolis, S.; Ioakim, C.; Papatheodorou, G.; Ferentinos, G. Short-Term Climate Changes in the Southern Aegean Sea over the Last 48,000 Years. *Palaeogeogr. Palaeoclimatol. Palaeoecol.* **2005**, *220*, 311–332. [\[CrossRef\]](#)
19. Geraga, M.; Ioakim, C.; Lykousis, V.; Tsaila-monopolis, S.; Mylona, G. The High-Resolution Palaeoclimatic and Palaeoceanographic History of the Last 24,000 Years in the Central Aegean Sea, Greece. *Palaeogeogr. Palaeoclimatol. Palaeoecol.* **2010**, *287*, 101–115. [\[CrossRef\]](#)
20. Kouli, K.; Gogou, A.; Bouloubassi, I.; Triantaphyllou, M.V.; Ioakim, C.; Katsouras, G.; Roussakis, G.; Lykousis, V. Late Postglacial Paleoenvironmental Change in the Northeastern Mediterranean Region: Combined Palynological and Molecular Biomarker Evidence. *Quat. Int.* **2012**, *261*, 118–127. [\[CrossRef\]](#)
21. Triantaphyllou, M.V.; Gogou, A.; Dimiza, M.D.; Kostopoulou, S.; Parinos, C.; Roussakis, G.; Geraga, M.; Bouloubassi, I.; Fleitmann, D.; Zervakis, V.; et al. Holocene Climatic Optimum Centennial-Scale Paleooceanography in the NE Aegean (Mediterranean Sea). *Geo-Mar. Lett.* **2016**, *36*, 51–66. [\[CrossRef\]](#)
22. Sondi, I.; Mikac, N.; Vdović, N.; Ivanić, M.; Furdek, M.; Škapin, S.D. Geochemistry of Recent Aragonite-Rich Sediments in Mediterranean Karstic Marine Lakes: Trace Elements as Pollution and Palaeoredox Proxies and Indicators of Authigenic Mineral Formation. *Chemosphere* **2017**, *168*, 786–797. [\[CrossRef\]](#)
23. Lambeck, K.; Rouby, H.; Purcell, A.; Sun, Y.; Sambridge, M. Sea Level and Global Ice Volumes from the Last Glacial Maximum to the Holocene. *Proc. Natl. Acad. Sci. USA* **2014**, *111*, 15296–15303. [\[CrossRef\]](#) [\[PubMed\]](#)
24. Lambeck, K.; Purcell, A. Sea-Level Change in the Mediterranean Sea since the LGM: Model Predictions for Tectonically Stable Areas. *Quat. Sci. Rev.* **2005**, *24*, 1969–1988. [\[CrossRef\]](#)
25. Sivan, D.; Wdowinski, S.; Lambeck, K.; Galili, E.; Raban, A. Holocene Sea-Level Changes along the Mediterranean Coast of Israel, Based on Archaeological Observations and Numerical Model. *Palaeogeogr. Palaeoclimatol. Palaeoecol.* **2001**, *167*, 101–117. [\[CrossRef\]](#)
26. Perdue, E.M.; Koprivnjak, J.-F. Using the C/N Ratio to Estimate Terrigenous Inputs of Organic Matter to Aquatic Environments. *Estuar. Coast. Shelf Sci.* **2007**, *73*, 65–72. [\[CrossRef\]](#)
27. Desruelles, S.; Fouache, É.; Ciner, A.; Dalongeville, R.; Pavlopoulos, K.; Kosun, E.; Coquinot, Y.; Potdevin, J.L. Beachrocks and Sea Level Changes since Middle Holocene: Comparison between the Insular Group of Mykonos-Delos-Rhenia (Cyclades, Greece) and the Southern Coast of Turkey. *Glob. Planet. Chang.* **2009**, *66*, 19–33. [\[CrossRef\]](#)
28. Pavlopoulos, K.; Theodorakopoulou, K. Relative Sea-Level Changes in Aegean Coastal Areas during Holocene: A Geoarchaeological View. *J. Earth Sci.* **2010**, *21*, 244–246.
29. Evelpidou, N.; Pavlopoulos, K.; Vassilopoulos, A.; Triantaphyllou, M.; Vouvalidis, K.; Syrides, G. Yria (Western Naxos Island, Greece): Sea Level Changes in Upper Holocene and Palaeogeographical Reconstruction. *Geodin. Acta* **2010**, *23*, 233–240. [\[CrossRef\]](#)
30. Emmanouilidis, A.; Unkel, I.; Seguin, J.; Keklikoglou, K.; Gianni, E.; Avramidis, P. Application of Non-Destructive Techniques on a Varve Sediment Record from Vouliagmeni Coastal Lake, Eastern Gulf of Corinth, Greece. *Appl. Sci.* **2020**, *10*, 8273. [\[CrossRef\]](#)
31. Vött, A. Relative Sea Level Changes and Regional Tectonic Evolution of Seven Coastal Areas in NW Greece since the Mid-Holocene. *Quat. Sci. Rev.* **2007**, *26*, 894–919. [\[CrossRef\]](#)
32. Sergiou, S.; Geraga, M.; Rohling, E.J.; Rodríguez-Sanz, L.; Hadjisolomou, E.; Paraschos, F.; Sakellariou, D.; Bailey, G. Influences of Sea Level Changes and the South Asian Monsoon on Southern Red Sea Oceanography over the Last 30 Ka. *Quat. Res.* **2022**, 1–19. [\[CrossRef\]](#)
33. Triantaphyllou, M.V.; Gogou, A.; Bouloubassi, I.; Dimiza, M.; Kouli, K.; Rousakis, G.; Kotthoff, U.; Emeis, K.C.; Papanikolaou, M.; Athanasiou, M.; et al. Evidence for a Warm and Humid Mid-Holocene Episode in the Aegean and Northern Levantine Seas (Greece, NE Mediterranean). *Reg. Environ. Chang.* **2014**, *14*, 1697–1712. [\[CrossRef\]](#)
34. Haghani, S.; Leroy, S.A.G.; Wesselingh, F.P.; Rose, N.L. Rapid Evolution of Coastal Lagoons in Response to Human Interference under Rapid Sea Level Change: A South Caspian Sea Case Study. *Quat. Int.* **2016**, *408*, 93–112. [\[CrossRef\]](#)
35. Koutsodendris, A.; Brauer, A.; Zacharias, I.; Putyrskaya, V.; Klemm, E.; Sangiorgi, F.; Pross, J. Ecosystem Response to Human- and Climate-Induced Environmental Stress on an Anoxic Coastal Lagoon (Etoliko, Greece) since 1930 AD. *J. Paleolimnol.* **2015**, *53*, 255–270. [\[CrossRef\]](#)
36. Papazachos, B.C. Seismicity of the Aegean and Surrounding Area. *Tectonophysics* **1990**, *178*, 287–308. [\[CrossRef\]](#)
37. Zweng, M.M.; Reagan, J.R.; Seidov, D.; Boyer, T.P.; Locarnini, R.A.; Garcia, H.E.; Mishonov, A.V.; Baranova, O.K.; Weathers, K.W.; Paver, C.R.; et al. *World Ocean Atlas 2018, Volume 2: Salinity*; NOAA Atlas NESDIS 82; A. Mishonov, Technical Editor: Silver Spring, MD, USA, 2019; p. 50.
38. Vlachopoulos, A. Excavation at vathy of astypalea island. In Proceedings of the Athenian Archaeological Society, Athens, Greece, 16 January 2016; pp. 328–356.
39. Berger, J.-F.; Lespez, L.; Kuzucuoğlu, C.; Glais, A.; Hourani, F.; Barra, A.; Guilaine, J. Interactions between Climate Change and Human Activities during the Early to Mid-Holocene in the Eastern Mediterranean Basins. *Clim. Past* **2016**, *12*, 1847–1877. [\[CrossRef\]](#)
40. Bailey, G.N.; Flemming, N.C. Archaeology of the Continental Shelf: Marine Resources, Submerged Landscapes and Underwater Archaeology. *Quat. Sci. Rev.* **2008**, *27*, 2153–2165. [\[CrossRef\]](#)
41. Theocharis, A.; Balopoulos, E.; Kioroglou, S.; Kontoyiannis, H.; Iona, A. A Synthesis of the Circulation and Hydrography of the South Aegean Sea and the Straits of the Cretan Arc (March 1994–January 1995). *Prog. Oceanogr.* **1999**, *44*, 469–509. [\[CrossRef\]](#)
42. Zervakis, V.; Georgopoulos, D.; Drakopoulos, P.G. The Role of the North Aegean in Triggering the Recent Eastern Mediterranean Climatic Changes. *J. Geophys. Res. Ocean.* **2000**, *105*, 26103–26116. [\[CrossRef\]](#)

43. Lykousis, V.; Chronis, G.; Tselepidis, A.; Price, N.B.; Theocharis, A.; Siokou-Frangou, I.; Van Wambeke, F.; Danovaro, R.; Stavrakakis, S.; Duineveld, G.; et al. Major Outputs of the Recent Multidisciplinary Biogeochemical Researches Undertaken in the Aegean Sea. *J. Mar. Syst.* **2002**, *33–34*, 313–334. [\[CrossRef\]](#)
44. Poulos, E.; Ghionis, G.; Maroukian, H. Geomorphology Sea-Level Rise Trends in the Attico—Cycladic Region (Aegean Sea) during the Last 5000 Years. *Geomorphology* **2009**, *107*, 10–17. [\[CrossRef\]](#)
45. Stavrakakis, S.; Chronis, G.; Tselepidis, A.; Heussner, S.; Monaco, A.; Abassi, A. Downward Fluxes of Settling Particles in the Deep Cretan Sea (NE Mediterranean). *Prog. Oceanogr.* **2000**, *46*, 217–240. [\[CrossRef\]](#)
46. Lykousis, V. Submarine Slope Instabilities in the Hellenic Arc Region, Northeastern Mediterranean Sea. *Mar. Geotechnol.* **1991**, *10*, 83–96. [\[CrossRef\]](#)
47. Piper, D.J.W.; Perissoratis, C. Late Quaternary Sedimentation on the North Aegean Continental Margin, Greece 1. *Am. Assoc. Pet. Geol. Bull.* **1991**, *75*, 46–61. [\[CrossRef\]](#)
48. Perissoratis, C.; Conispoliatis, N. The Impacts of Sea-Level Changes during Latest Pleistocene and Holocene Times on the Morphology of the Ionian and Aegean Seas (SE Alpine Europe). *Mar. Geol.* **2003**, *196*, 145–156. [\[CrossRef\]](#)
49. Pavlides, S.; Caputo, R. Magnitude versus Faults' Surface Parameters: Quantitative Relationships from the Aegean Region. *Tectonophysics* **2004**, *380*, 159–188. [\[CrossRef\]](#)
50. Lykousis, V.; Karageorgis, A.P.; Chronis, G.T. Delta Progradation and Sediment Fluxes since the Last Glacial in the Thermaikos Gulf and the Sporades Basin, NW Aegean Sea, Greece. *Mar. Geol.* **2005**, *222–223*, 381–397. [\[CrossRef\]](#)
51. Lykousis, V. Sea-Level Changes and Shelf Break Prograding Sequences during the Last 400 Ka in the Aegean Margins: Subsidence Rates and Palaeogeographic Implications. *Cont. Shelf Res.* **2009**, *29*, 2037–2044. [\[CrossRef\]](#)
52. Tsampouraki-Kraounaki, K.; Sakellariou, D.; Rousakis, G.; Morfis, I.; Panagiotopoulos, I.; Livanos, I.; Manta, K.; Paraschos, F.; Papatheodorou, G. The Santorini-Amorgos Shear Zone: Evidence for Dextral Transtension in the South Aegean Back-Arc Region, Greece. *Geosciences* **2021**, *11*, 216. [\[CrossRef\]](#)
53. Nomikou, P.; Hübscher, C.; Papanikolaou, D.; Farangitakis, G.P.; Ruhnau, M.; Lampridou, D. Expanding Extension, Subsidence and Lateral Segmentation within the Santorini-Amorgos Basins during Quaternary: Implications for the 1956 Amorgos Events, Central-South Aegean Sea, Greece. *Tectonophysics* **2018**, *722*, 138–153. [\[CrossRef\]](#)
54. Blott, S.J.; Pye, K. GRADISTAT: A grain size distribution and statistics package for the analysis of unconsolidated sediments. *Tech. Commun.* **2001**, *1248*, 1237–1248. [\[CrossRef\]](#)
55. van Santvoort, P.J.M.; de Lange, G.J.; Thomson, J.; Cussen, H.; Wilson, T.R.S.; Krom, M.D.; Ströhle, K. Active Post-Depositional Oxidation of the Most Recent Sapropel (S1) in Sediments of the Eastern Mediterranean Sea. *Geochim. Cosmochim. Acta* **1996**, *60*, 4007–4024. [\[CrossRef\]](#)
56. Nagao, S.; Nakashima, S. The Factors Controlling Vertical Color Variations of North Atlantic Madeira Abyssal Plain Sediments. *Mar. Geol.* **1992**, *109*, 83–94. [\[CrossRef\]](#)
57. Wu, L.; Wang, R.; Krijgsman, W.; Chen, Z.; Xiao, W.; Ge, S.; Wu, J. Deciphering Color Reflectance Data of a 520-Kyr Sediment Core From the Southern Ocean: Method Application and Paleoenvironmental Implications. *Geochem. Geophys. Geosyst.* **2019**, *20*, 2808–2826. [\[CrossRef\]](#)
58. Giosan, L.; Flood, R.D.; Aller, R.C. Paleooceanographic Significance of Sediment Color on Western North Atlantic Drifts: I. Origin of Color. *Mar. Geol.* **2002**, *189*, 25–41. [\[CrossRef\]](#)
59. Weltje, G.J.; Bloemsa, M.R.; Tjallingii, R.; Heslop, D.; Röhl, U.; Croudace, I.W.; Croudace, I.W. *Prediction of Geochemical Composition from XRF Core Scanner Data: A New Multivariate Approach Including Automatic Selection of Calibration Samples and Quantification of Uncertainties*; Developments in Paleoenvironmental Research Book Series; Springer: Berlin/Heidelberg, Germany, 2015; Volume 17, pp. 507–534. [\[CrossRef\]](#)
60. Heslop, D.; Dillon, M. Unmixing Magnetic Remanence Curves without a Priori Knowledge. *Geophys. J. Int.* **2007**, *170*, 556–566. [\[CrossRef\]](#)
61. Ji, S.; Xingqi, L.; Sumin, W.; Matsumoto, R. Palaeoclimatic Changes in the Qinghai Lake Area during the Last 18,000 Years. *Quat. Int.* **2005**, *136*, 131–140. [\[CrossRef\]](#)
62. Rein, B.; Sirocko, F. In-Situ Reflectance Spectroscopy—Analysing Techniques for High-Resolution Pigment Logging in Sediment Cores. *Int. J. Earth Sci.* **2002**, *91*, 950–954. [\[CrossRef\]](#)
63. Heaton, T.J.; Köhler, P.; Butzin, M.; Bard, E.; Reimer, R.W.; Austin, W.E.N.; Bronk Ramsey, C.; Grootes, P.M.; Hughen, K.A.; Kromer, B.; et al. Marine20—The Marine Radiocarbon Age Calibration Curve (0–55,000 Cal BP). *Radiocarbon* **2020**, *62*, 779–820. [\[CrossRef\]](#)
64. Marino, G.; Rohling, E.J.; Sangiorgi, F.; Hayes, A.; Casford, J.L.; Lotter, A.F.; Kucera, M.; Brinkhuis, H. Early and Middle Holocene in the Aegean Sea: Interplay between High and Low Latitude Climate Variability. *Quat. Sci. Rev.* **2009**, *28*, 3246–3262. [\[CrossRef\]](#)
65. Blaauw, M.; Christen, J.A. Flexible Paleoclimate Age-Depth Models Using an Autoregressive Gamma Process. *Bayesian Anal.* **2011**, *6*, 457–474. [\[CrossRef\]](#)
66. Mook, W.G.; van der Plicht, J. Reporting ¹⁴C Activities and Concentrations. *Radiocarbon* **1999**, *41*, 227–239. [\[CrossRef\]](#)
67. Kinsman, D.J.J. Interpretation of Sr (Super +2) Concentrations in Carbonate Minerals and Rocks. *J. Sediment. Res.* **1969**, *39*, 486–508. [\[CrossRef\]](#)

68. Rothwell, R.G.; Hoogakker, B.; Thomson, J.; Croudace, I.W.; Frenz, M. Turbidite Emplacement on the Southern Balearic Abyssal Plain (Western Mediterranean Sea) during Marine Isotope Stages 1–3: An Application of ITRAX XRF Scanning of Sediment Cores to Lithostratigraphic Analysis. *Geol. Soc. London Spec. Publ.* **2006**, *267*, 79–98. [\[CrossRef\]](#)
69. Wilkinson, B.H.; Given, R.K. Secular Variation in Abiotic Marine Carbonates: Constraints on Phanerozoic Atmospheric Carbon Dioxide Contents and Oceanic Mg/Ca Ratios. *J. Geol.* **1986**, *94*, 321–333. [\[CrossRef\]](#)
70. Kelts, K.; Hsü, K.J. Freshwater Carbonate Sedimentation. In *Lakes*; Springer: New York, NY, USA, 1978; pp. 295–323. [\[CrossRef\]](#)
71. Bayon, G.; Pierre, C.; Etoubleau, J.; Voisset, M.; Cauquil, E.; Marsset, T.; Sultan, N.; Le Drezen, E.; Fouquet, Y. Sr/Ca and Mg/Ca Ratios in Niger Delta Sediments: Implications for Authigenic Carbonate Genesis in Cold Seep Environments. *Mar. Geol.* **2007**, *241*, 93–109. [\[CrossRef\]](#)
72. De Choudens-Sánchez, V.; Gonzalez, L.A. Calcite and Aragonite Precipitation Under Controlled Instantaneous Supersaturation: Elucidating the Role of CaCO₃ Saturation State and Mg/Ca Ratio on Calcium Carbonate Polymorphism. *J. Sediment. Res.* **2009**, *79*, 363–376. [\[CrossRef\]](#)
73. Sondi, I.; Juračić, M. Whiting Events and the Formation of Aragonite in Mediterranean Karstic Marine Lakes: New Evidence on Its Biologically Induced Inorganic Origin. *Sedimentology* **2010**, *57*, 85–95. [\[CrossRef\]](#)
74. Meyers, P.A. Lacustrine Organic Geochemistry—An Overview of Indicators of Organic Matter Sources and Diagenesis in Lake Sediments. *Org. Geochem.* **1993**, *20*, 867–900. [\[CrossRef\]](#)
75. Meyers, P.A. Preservation of Elemental and Isotopic Source Identification of Sedimentary Organic Matter. *Chem. Geol.* **1994**, *114*, 289–302. [\[CrossRef\]](#)
76. Fuksi, T.; Tomašovych, A.; Gallmetzer, I.; Haselmair, A.; Zuschin, M. 20th Century Increase in Body Size of a Hypoxia-Tolerant Bivalve Documented by Sediment Cores from the Northern Adriatic Sea (Gulf of Trieste). *Mar. Pollut. Bull.* **2018**, *135*, 361–375. [\[CrossRef\]](#)
77. Leontarakis, P.K.; Xatzianastasiou, L.I.; Theodorou, J.A. Biological Aspects of the Lagoon Cockle, *Cerastoderma Glaucum* (Poiret 1879), in a Coastal Lagoon in Keramoti, Greece in the Northeastern Mediterranean. *J. Shellfish Res.* **2008**, *27*, 1171–1175. [\[CrossRef\]](#)
78. Debenay, J.-P.; Payri, C.E. Epiphytic foraminiferal assemblages on macroalgae in reefal environments of new caledonia. *J. Foraminifer. Res.* **2010**, *40*, 36–60. [\[CrossRef\]](#)
79. Barmawidjaja, D.M.; Van der Zwaan, G.J.; Jorissen, F.J.; Puskaric, S. 150 Years of Eutrophication in the Northern Adriatic Sea: Evidence from a Benthic Foraminiferal Record. *Mar. Geol.* **1995**, *122*, 367–384. [\[CrossRef\]](#)
80. Faber, W.W. Distribution and Substrate Preference of *Peneroplis Planatus* and *P. Arientinus* from the Halophia Meadow near Wadi Taba, Eilat, Israel. *J. Foraminifer. Res.* **1991**, *21*, 218–221. [\[CrossRef\]](#)
81. Frontalini, F.; Coccioni, R. Benthic Foraminifera as Bioindicators of Pollution: A Review of Italian Research over the Last Three Decades. *Rev. Micropaleontol.* **2011**, *54*, 115–127. [\[CrossRef\]](#)
82. Jorissen, F.; Nardelli, M.P.; Almogi-Labin, A.; Barras, C.; Bergamin, L.; Bicchi, E.; El Kateb, A.; Ferraro, L.; McGann, M.; Morigi, C.; et al. Developing Foraminiferal AMBI for Biomonitoring in the Mediterranean: Species Assignments to Ecological Categories. *Mar. Micropaleontol.* **2018**, *140*, 33–45. [\[CrossRef\]](#)
83. Dimiza, M.D.; Triantaphyllou, M.V.; Koukousioura, O.; Hallock, P.; Simbhora, N.; Karageorgis, A.P.; Papathanasiou, E. The Foraminiferal Stress Index: A New Tool for Environmental Assessment of Soft-Bottom Environments Using Benthic Foraminifera. A Case Study from the Saronikos Gulf, Greece, Eastern Mediterranean. *Ecol. Indic.* **2016**, *60*, 611–621. [\[CrossRef\]](#)
84. Khanaqa, P.A.; Karim, K.H.; Thiel, V. Characeae-Derived Carbonate Deposits in Lake Ganau, Kurdistan Region, Iraq. *Facies* **2013**, *59*, 653–662. [\[CrossRef\]](#)
85. Murray, J.W. *Ecology and Applications of Benthic Foraminifera*; Cambridge University Press: Cambridge, UK, 2006; ISBN 0521828392.
86. Scourse, J.D.; Kennedy, H.; Scott, G.A.; Austin, W.E.N. Stable Isotopic Analyses of Modern Benthic Foraminifera from Seasonally Stratified Shelf Seas: Disequilibria and the “Seasonal Effect”. *Holocene* **2004**, *14*, 747–758. [\[CrossRef\]](#)
87. Austin, W.E.N.; Scourse, J.D. Evolution of Seasonal Stratification in the Celtic Sea during the Holocene. *J. Geol. Soc. London* **1997**, *154*, 249–256. [\[CrossRef\]](#)
88. Scourse, J.D.; Austin, W.E.N.; Long, B.T.; Assinder, D.J.; Huws, D. Holocene Evolution of Seasonal Stratification in the Celtic Sea: Refined Age Model, Mixing Depths and Foraminiferal Stratigraphy. *Mar. Geol.* **2002**, *191*, 119–145. [\[CrossRef\]](#)
89. Woods, M.A.; Wilkinson, I.P.; Leng, M.J.; Riding, J.B.; Vane, C.H.; Lopes dos Santos, R.A.; Kender, S.; De Schepper, S.; Hennissen, J.A.I.; Ward, S.L.; et al. Tracking Holocene Palaeostratification and Productivity Changes in the Western Irish Sea: A Multi-Proxy Record. *Palaeogeogr. Palaeoclimatol. Palaeoecol.* **2019**, *532*, 109231. [\[CrossRef\]](#)
90. Grossman, E.L. Carbon Isotopic Fractionation in Live Benthic Foraminifera—Comparison with Inorganic Precipitate Studies. *Geochim. Cosmochim. Acta* **1984**, *48*, 1505–1512. [\[CrossRef\]](#)
91. McCorkle, D.C.; Keigwin, L.D.; Corliss, B.H.; Emerson, S.R. The Influence of Microhabitats on the Carbon Isotopic Composition of Deep-Sea Benthic Foraminifera. *Paleoceanography* **1990**, *5*, 161–185. [\[CrossRef\]](#)
92. McCorkle, D.C.; Corliss, B.H.; Farnham, C.A. Vertical Distributions and Stable Isotopic Compositions of Live (Stained) Benthic Foraminifera from the North Carolina and California Continental Margins. *Deep Sea Res. Part I Oceanogr. Res. Pap.* **1997**, *44*, 983–1024. [\[CrossRef\]](#)
93. Rathburn, A.E.; Corliss, B.H.; Tappa, K.D.; Lohmann, K.C. Comparisons of the Ecology and Stable Isotopic Compositions of Living (Stained) Benthic Foraminifera from the Sulu and South China Seas. *Deep Sea Res. Part I Oceanogr. Res. Pap.* **1996**, *43*, 1617–1646. [\[CrossRef\]](#)

94. Mackensen, A.; Wollenburg, J.; Licari, L. Methane Venting Documented by Lowest Hitherto Reported $\delta^{13}\text{C}$ of Live Epibenthic Foraminifer *Fontbotia Wuellerstorfi*. In Proceedings of the AGU Fall Meeting Abstracts, San Francisco, CA, USA, 13–17 December 2004; Volume 2004, pp. PP23B–1437.
95. Fontanier, C.; Mackensen, A.; Jorissen, F.J.; Anschutz, P.; Licari, L.; Griveaud, C. Stable Oxygen and Carbon Isotopes of Live Benthic Foraminifera from the Bay of Biscay: Microhabitat Impact and Seasonal Variability. *Mar. Micropaleontol.* **2006**, *58*, 159–183. [\[CrossRef\]](#)
96. Schmiedl, G.; Pfeilsticker, M.; Hemleben, C.; Mackensen, A. Environmental and Biological Effects on the Stable Isotope Composition of Recent Deep-Sea Benthic Foraminifera from the Western Mediterranean Sea. *Mar. Micropaleontol.* **2004**, *51*, 129–152. [\[CrossRef\]](#)
97. Martin, G.; Torn, K.; Blindow, I.; Schubert, H.; Munsterhjelm, R.; Henricson, C. Introduction to Charophytes. In *Charophytes of the Baltic Sea*; Schubert, H., Blindow, I., Eds.; Gantner Verlag: Starnberg, Germany, 2003; Volume 19, pp. 3–14.
98. Roeser, P.; Franz, S.O.; Litt, T. Aragonite and Calcite Preservation in Sediments from Lake Iznik Related to Bottom Lake Oxygenation and Water Column Depth. *Sedimentology* **2016**, *63*, 2253–2277. [\[CrossRef\]](#)
99. Schemmel, F.; Niedermeyer, E.M.; Koutsodendris, A.; Pross, J.; Fiebig, J.; Mulch, A. Paleohydrological Changes in the Eastern Mediterranean Region during the Early to Mid-Holocene Recorded in Plant Wax n-Alkane Distributions and $\Delta^{13}\text{C}$ TOC—New Data from Tenaghi Philippon, NE Greece. *Org. Geochem.* **2017**, *110*, 100–109. [\[CrossRef\]](#)
100. Cheng, H.; Sinha, A.; Verheyden, S.; Nader, F.H.; Li, X.L.; Zhang, P.Z.; Yin, J.J.; Yi, L.; Peng, Y.B.; Rao, Z.G.; et al. The Climate Variability in Northern Levant over the Past 20,000 Years. *Geophys. Res. Lett.* **2015**, *42*, 8641–8650. [\[CrossRef\]](#)
101. Ariztegui, D.; Anselmetti, F.S.; Robbiani, J.M.; Bernasconi, S.M.; Brati, E.; Gilli, A.; Lehmann, M.F. Natural and Human-Induced Environmental Change in Southern Albania for the Last 300 Years—Constraints from the Lake Butrint Sedimentary Record. *Glob. Planet. Chang.* **2010**, *71*, 183–192. [\[CrossRef\]](#)
102. Clarke, J.; Brooks, N.; Banning, E.B.; Bar-Matthews, M.; Campbell, S.; Clare, L.; Cremaschi, M.; di Lernia, S.; Drake, N.; Gallinaro, M.; et al. Climatic Changes and Social Transformations in the Near East and North Africa during the ‘Long’ 4th Millennium BC: A Comparative Study of Environmental and Archaeological Evidence. *Quat. Sci. Rev.* **2016**, *136*, 96–121. [\[CrossRef\]](#)
103. Ben Dor, Y.; Neugebauer, I.; Enzel, Y.; Schwab, M.J.; Tjallingii, R.; Erel, Y.; Brauer, A. Varves of the Dead Sea Sedimentary Record. *Quat. Sci. Rev.* **2019**, *215*, 173–184. [\[CrossRef\]](#)
104. Vail, P.R.; Mitchum, R.M., Jr.; Thompson, S., III. Seismic Stratigraphy and Global Changes of Sea Level, Part 3: Relative Changes of Sea Level from Coastal Onlap. In *Seismic Stratigraphy—Applications to Hydrocarbon Exploration*; Payton, C.E., Ed.; American Association of Petroleum Geologists: Tulsa, OK, USA, 1997; Volume 26. [\[CrossRef\]](#)
105. Piper, D.J.W.; Perissoratis, C. Quaternary Neotectonics of the South Aegean arc. *Mar. Geol.* **2003**, *198*, 259–288. [\[CrossRef\]](#)
106. Spratt, R.M.; Lisiecki, L.E. A Late Pleistocene Sea Level Stack. *Clim. Past* **2016**, *12*, 1079–1092. [\[CrossRef\]](#)
107. Karkani, A.; Evelpidou, N.; Tzouxanioti, M.; Petropoulos, A.; Gogou, M.; Mloukie, E. Tsunamis in the Greek Region: An Overview of Geological and Geomorphological Evidence. *Geosciences* **2022**, *12*, 4. [\[CrossRef\]](#)
108. De Lange, G.J.; Thomson, J.; Reitz, A.; Slomp, C.P.; Speranza Principato, M.; Erba, E.; Corselli, C. Synchronous Basin-Wide Formation and Redox-Controlled Preservation of a Mediterranean Sapropel. *Nat. Geosci.* **2008**, *1*, 606–610. [\[CrossRef\]](#)
109. Incarbona, A.; Abu-Zied, R.H.; Rohling, E.J.; Ziveri, P. Reventilation Episodes During the Sapropel S1 Deposition in the Eastern Mediterranean Based on Holococcolith Preservation. *Paleoceanogr. Paleoclimatol.* **2019**, *34*, 1597–1609. [\[CrossRef\]](#)
110. López-Merino, L.; Leroy, S.A.G.; Eshel, A.; Epshtein, V.; Belmaker, R.; Bookman, R. Using Palynology to Re-Assess the Dead Sea Laminated Sediments—Indeed Varves? *Quat. Sci. Rev.* **2016**, *140*, 49–66. [\[CrossRef\]](#)
111. Morellón, M.; Anselmetti, F.S.; Ariztegui, D.; Brushliti, B.; Sinopoli, G.; Wagner, B.; Sadori, L.; Gilli, A.; Pambuku, A. Human-Climate Interactions in the Central Mediterranean Region during the Last Millennia: The Laminated Record of Lake Butrint (Albania). *Quat. Sci. Rev.* **2016**, *136*, 134–152. [\[CrossRef\]](#)
112. Perissoratis, C.; Piper, D.J.W. Age, Regional Variation, and Shallowest Occurrence of S1 Sapropel in the Northern Aegean Sea. *Geo-Mar. Lett.* **1992**, *12*, 49–53. [\[CrossRef\]](#)
113. Çağatay, M.N.; Eriş, K.; Ryan, W.B.F.; Sancar, Ü.; Polonia, A.; Akçer, S.; Biltekin, D.; Gasperini, L.; Görür, N.; Lericolais, G.; et al. Late Pleistocene–Holocene Evolution of the Northern Shelf of the Sea of Marmara. *Mar. Geol.* **2009**, *265*, 87–100. [\[CrossRef\]](#)
114. Marino, G.; Rohling, E.J.; Rijpstra, W.I.C.; Sangiorgi, F.; Schouten, S.; Damsté, J.S.S. Aegean Sea as Driver of Hydrographic and Ecological Changes in the Eastern Mediterranean. *Geology* **2007**, *35*, 675–678. [\[CrossRef\]](#)
115. Rohling, E.J.; Cane, T.R.; Cooke, S.; Sprovieri, M.; Bouloubassi, I.; Emeis, K.C.; Schiebel, R.; Kroon, D.; Jorissen, F.J.; Lorre, A.; et al. African Monsoon Variability during the Previous Interglacial Maximum. *Earth Planet. Sci. Lett.* **2002**, *202*, 61–75. [\[CrossRef\]](#)
116. Bar-Matthews, M.; Ayalon, A.; Kaufman, A. Late Quaternary Paleoclimate in the Eastern Mediterranean Region from Stable Isotope Analysis of Speleothems at Soreq Cave, Israel. *Quat. Res.* **1997**, *47*, 155–168. [\[CrossRef\]](#)
117. Frisia, S.; Borsato, A.; Mangini, A.; Spötl, C.; Madonia, G.; Sauro, U. Holocene Climate Variability in Sicily from a Discontinuous Stalagmite Record and the Mesolithic to Neolithic Transition. *Quat. Res.* **2006**, *66*, 388–400. [\[CrossRef\]](#)
118. Bar-Matthews, M.; Ayalon, A.; Kaufman, A. Middle to Late Holocene (6,500 Yr. Period) Paleoclimate in the Eastern Mediterranean Region from Stable Isotopic Composition of Speleothems from Soreq Cave, Israel. In *Water, Environment and Society in Times of Climatic Change*; Issar, A.S., Brown, N., Eds.; Springer: Dordrecht, The Netherlands, 1998; pp. 203–214, ISBN 978-94-017-3659-6.
119. Bar-Matthews, M.; Ayalon, A.; Kaufman, A.; Wasserburg, G.J. The Eastern Mediterranean Paleoclimate as a Reflection of Regional Events: Soreq Cave, Israel. *Earth Planet. Sci. Lett.* **1999**, *166*, 85–95. [\[CrossRef\]](#)

-
120. Grant, K.M.; Rohling, E.J.; Bar-Matthews, M.; Ayalon, A.; Medina-Elizalde, M.; Ramsey, C.B.; Satow, C.; Roberts, A.P. Rapid Coupling between Ice Volume and Polar Temperature over the Past 150,000 Years. *Nature* **2012**, *491*, 744–747. [[CrossRef](#)]
 121. Griggs, G. 1. Human Settlement of the Coastal Zone. In *Coasts in Crisis*; University of California Press: Berkeley, CA, USA, 2017; pp. 1–20.
 122. Devillers, B.; Bony, G.; Degeai, J.-P.; Gascò, J.; Lachenal, T.; Bruneton, H.; Yung, F.; Oueslati, H.; Thierry, A. Holocene coastal environmental changes and human occupation of the lower Hérault River, southern France. *Quat. Sci. Rev.* **2019**, *222*, 105912. [[CrossRef](#)]